Springer Series in Materials Science 156

Stephen Pearton *Editor*

GaN and ZnO-based Materials and Devices

Springer

Springer Series in
MATERIALS SCIENCE 156

Springer Series in

MATERIALS SCIENCE

The Springer Series in Materials Science covers the complete spectrum of materials physics, including fundamental principles, physical properties, materials theory and design. Recognizing the increasing importance of materials science in future device technologies, the book titles in this series reflect the state-of-the-art in understanding and controlling the structure and properties of all important classes of materials.

Please view available titles in *Springer Series in Materials Science*
on series homepage http://www.springer.com/series/856

Stephen Pearton
Editor

GaN and ZnO-based Materials and Devices

With 328 Figures

Springer

Editor
Stephen Pearton
University of Florida
Materials Science and Engineering
100 Rhines Hall, 32611 Gainesville, USA
spear@mse.ufl.edu

Springer Series in Materials Science ISSN 0933-033X
ISBN 978-3-642-23520-7 e-ISBN 978-3-642-23521-4
DOI 10.1007/978-3-642-23521-4
Springer Heidelberg Dordrecht London New York

Library of Congress Control Number: 2011945030

Printed on acid-free paper

Springer is part of Springer Science+Business Media (www.springer.com)

Preface

The GaN materials system has applications in visible and UV light emitting devices and in high power, high temperature electronics. On the photonics side, the AlGaInN materials system, consisting of AlGaN/GaN, InAlN/GaN, and InGaN/GaN heterostructures and the GaN, AlN, and InN binaries, is widely used in blue/violet/white/UV light emitting diodes for stoplights and full color displays, blue and green lasers for use in high-density CD-ROM storage and high-resolution printers. The main applications for GaN-based high power microwave transistors are in phased array radar systems and wireless communication systems, while the low noise, radiation hard transistors can be used in high temperature sensors and spaceflight instrumentation. There have been many recent advances in this field, concerning sensors and nanostructure synthesis. Functional nanostructures are attracting much interest for use in sensing, energy harvesting and cell monitoring. In addition, there is a widespread interest in the use of ZnO in UV light emitters and flexible electronics. Flexible displays are attractive for portable devices such as smart phones, laptops, e-books, and wearable devices due to their lightweight, low power consumption, and being bendable. In defense applications, soldiers can use flexible display computers on the battlefield for communication and information access. Thin-film transistors (TFTs) are field effect transistors made by depositing thin films of amorphous Si, organics, or new inorganics based on ZnO for the semiconductor active layer. The channel region of a TFT is deposited onto a substrate such as glass, since the main market is in liquid crystal displays (LCDs). Since these types of substrates do not allow for high temperature processing, the TFT active region must be deposited at low temperature. Recently, indium zinc oxides (IZO) such as 90 wt% In_2O_3–10 wt% ZnO and homogeneous $In_2O_3(ZnO)_k$ ($k = 2, 3, 4, 5, 6, 7, 9, 11, 13,$ and 15) compounds have attracted significant attention as new candidates for transparent electrodes due to their good conductivity, high optical transparency, excellent surface smoothness, and low deposition temperature. One of the major challenges in the development of transparent thin-film transistors is to control the carrier concentration with high transparency in the active channel. For active channel materials, oxide semiconductors such as ZnO, $(ZnO)_x(SnO_2)_{1-x}$, 90 wt% In_2O_3–10 wt% ZnO, $In_2O_3(ZnO)_2$, and $InGaZnO_4$ have been reported to

be as alternatives to α-Si:H in thin-film transistors. Recent results have shown that InZnO has high electron mobility even for room temperature deposition, allowing for use of cheap substrates such as glass for fabrication of TFTs with superior performance to a-Si(H)TFTs.

This book brings together experts in both the GaN and ZnO areas to provide the most up-to-date information on advances in these fields. The topics begin with growth of advanced III-Nitride structures, specifically non-polar growth and high Al content alloys, leading into devices such as green and UV LEDs, HEMT power devices, and sensors. Advances in nitride nanostructures and understanding of radiation defects in GaN are covered, followed by reviews of developments in synthesis and control of ZnO-based films and nanostructures. Finally, the use of amorphous, transparent conducting oxides for channels in TFTs on novel substrates is reviewed. The purpose of the book is to provide both a summary of the current state-of-the-art and directions for future research.

Gainesville, FL, USA *S.J. Pearton*
December 2011

Contents

Contributors

Pedro Barquinha CENIMAT-I3N, Departamento de Ciência dos Materiais, and CEMOP/UNINOVA, Faculdade de Ciências e Tecnologia, FCT, Universidade Nova de Lisboa, 2829-516, Caparica, Portugal

Xian-An (Andrew) Cao West Virginia University, Lane Department of Computer Science and Electrical Engineering, Morgantown, WV 26506-6070, USA, xacao@mail.wvu.edu

C.Y. Chang University of Florida, Department of Chemical Engineering, Gainesville, FL 32611, USA

K.H. Chen University of Florida, Department of Chemical Engineering, Gainesville, FL 32611, USA

Ruei-San Chen Graduate Institute of Applied Technology, National Taiwan University of Science and Technology, Taipei 106, Taiwan

Li-Chyong Chen Center for Condensed Matter Sciences, National Taiwan University, Taipei 106, Taiwan, chenkh@pub.iams.sinica.edu.tw

Victor Chen University of Florida, Department of Chemical Engineering, Gainesville, FL 32611, USA

H. Chen Department of Electrical and Computer Engineering, Rutgers University, 94 Brett Road, Piscataway, NJ 0885, USA

Leonid Chernyak Department of Physics, University of Central Florida, Orlando, FL 32816, USA, chernyak@physics.ucf.edu

T. Paul Chow Department of Electrical, Computer and Systems Engineering, Rensselaer Polytechnic Institute, Troy, NY 12180, USA, chowt@rpi.edu

B.H. Chu University of Florida, Department of Chemical Engineering, Gainesville, FL 32611, USA

Zinovy Dashevsky Department of Physics, University of Central Florida, Orlando, FL 32816, USA

Jeff Davis College of Physical and Mathematical Sciences, Australian National University, Canberra, ACT 0200, Australia

Alex Dobrinsky Sensor Electronic Technology, Inc., Columbia, SC 29209, USA, adobrinsky@s-et.com

Elena Flitsyian Department of Physics, University of Central Florida, Orlando, FL 32816, USA

Elvira Fortunato CENIMAT-I3N, Departamento de Ciência dos Materiais,
and
CEMOP/UNINOVA, Faculdade de Ciências e Tecnologia, FCT, Universidade Nova de Lisboa, 2829-516, Caparica, Portugal, elvira-fortunato@fct.unl.pt

Abhijit Ganguly Center for Condensed Matter Sciences, National Taiwan University, Taipei 106, Taiwan

Remis Gaska Sensor Electronic Technology, Inc., Columbia, SC 29209, USA

Jung Han Department of Electrical Engineering, Yale University, 15 Prospect Street, BCT 517, New Haven, CT 06511, USA, jung.han@yale.edu

Kuei-Hsien Center for Condensed Matter Sciences, National Taiwan University, Taipei 106, Taiwan, Chen chenlc@ntu.edu.tw
and
Institute of Atomic and Molecular Sciences, Academia Sinica, Taipei 106, Taiwan

C. Jagadish College of Physical and Mathematical Sciences, Australian National University, Canberra, ACT 0200, Australia, Chennupati.Jagadish@anu.edu.au

Wayne Johnson Kopin Corporation, 125 North Drive, Westboro, MA 01581, USA, Wayne_Johnson@kopin.com

Hongxing Jiang Texas Tech University, Electrical and Computer Engineering Department, Lubbock, TX 79409-3102, USA, hx.jiang@ttu.edu

Jihyun Kim Department of Chemical and Biological Engineering, College of Engineering, Korea University, Anam-dong 5-1, Sungbuk-gu, Seoul 136-701, South Korea, hyunhyun7@korea.ac.kr

Z. Li Department of Electrical, Computer and Systems Engineering, Rensselaer Polytechnic Institute, Troy, NY 12180, USA

Jingyu Lin Texas Tech University, Electrical and Computer Engineering Department, Lubbock, TX 79409-3102, USA, jingyu.lin@ttu.edu

Yicheng Lu Department of Electrical and Computer Engineering, Rutgers University, 94 Brett Road, Piscataway, NJ 0885, USA, ylu@ece.rutgers.edu

Rodrigo Martins CENIMAT-I3N, Departamento de Ciência dos Materiais, and
CEMOP/UNINOVA, Faculdade de Ciências e Tecnologia, FCT, Universidade Nova de Lisboa, 2829-516 Caparica, Portugal

Edwin Piner Texas State University, San Marcos, Department of Physics, 601 University Dr., San Marcos, TX 78666, USA, epiner@txstate.edu

B.N. Pantha Texas Tech University, Electrical and Computer Engineering Department, Lubbock, TX 79409-3102, USA

S.J. Pearton Department of Materials Science and Engineering, University of Florida, Gainesville, FL 32611, USA, spear@mse.ufl.edu

Alexander Polyakov Institute of Rare Metals, B. Tolmachevsky 5, 119017 Moscow, Russia, aypolyakov@gmail.com

Fan Ren University of Florida, Department of Chemical Engineering, Gainesville, FL 32611, USA, ren@che.ufl.edu

P.I. Reyes Department of Electrical and Computer Engineering, Rutgers University, 94 Brett Road, Piscataway, NJ 0885, USA

Max Shatalov Sensor Electronic Technology, Inc., Columbia, SC 29209, USA

Michael Shur Department of Electrical, Computer and Systems Engineering, Rensselaer Polytechnic Institute, Troy, NY 12180, USA, shurm@rpi.edu

Michael Snure Nanostructured Materials Research Laboratory, Department of Materials Science and Engineering, University of Utah, Salt Lake City, UT 84112, USA

Paul Slusser Nanostructured Materials Research Laboratory, Department of Materials Science and Engineering, University of Utah, Salt Lake City, UT 84112, USA

Qian Sun Department of Electrical Engineering, Yale University, 15 Prospect Street, BCT 517, New Haven, CT 06511 USA

Ashutosh Tiwari Nanostructured Materials Research Laboratory, Department of Materials Science & Engineering, University of Utah, Salt Lake City, UT 84112, USA, tiwari@eng.utah.edu

David Toledo Nanostructured Materials Research Laboratory, Dept. of Materials Science & Engineering, University of Utah, Salt Lake City, UT 84112 USA

J. Zhong Department of Electrical and Computer Engineering, Rutgers University, 94 Brett Road, Piscataway, NJ 0885, USA

Chapter 1
Heteroepitaxy of Nonpolar and Semipolar GaN

Qian Sun and Jung Han

Abstract There has been increasing research interest in nonpolar and semipolar GaN for high brightness light-emitting diode (LED) and laser diode applications. Due to the very limited supply of GaN bulk substrates, the feasible way of obtaining cost-effective large-area nonpolar and semipolar GaN materials in the foreseeable future is still through heteroepitaxy on foreign substrates. The major challenge in the heteroepitaxy of nonpolar and semipolar GaN is the high density of stacking faults and partial dislocations, which are responsible for the poor performance of heteroepitaxial nonpolar and semipolar LEDs. This chapter presents kinetic Wulff plots (*v*-plots) of GaN as a novel and powerful methodology to understand and control GaN heteroepitaxy along various crystallographic orientations. Based on the *v*-plots, a two-step growth scheme is rationally designed and experimentally confirmed in reducing the defect density for nonpolar and semipolar GaN heteroepitaxy on planar substrates. A defect reduction model is proposed based on the correlation between the morphological evolution and the microstructural development. With the orientation of nucleation decoupled from the final film surface orientation, orientation controlled epitaxy has been demonstrated as a very promising approach for device quality nonpolar and semipolar GaN materials. The material research timeline of nonpolar and semipolar GaN is summarized and discussed.

1.1 Introduction

The discovery of a two-step growth procedure for the heteroepitaxy of GaN on *c*-plane sapphire [1, 2] is widely considered the key breakthrough for GaN-based materials and devices (Fig. 1.1). In the past two decades, the heteroepitaxy of GaN

Q. Sun · J. Han (✉)
Department of Electrical Engineering, Yale University, 15 Prospect Street, BCT 517, New Haven, CT 06511, USA
e-mail: qian.sun@aya.yale.edu; jung.han@yale.edu

S. Pearton (ed.), *GaN and ZnO-based Materials and Devices*,
Springer Series in Materials Science 156, DOI 10.1007/978-3-642-23521-4_1,

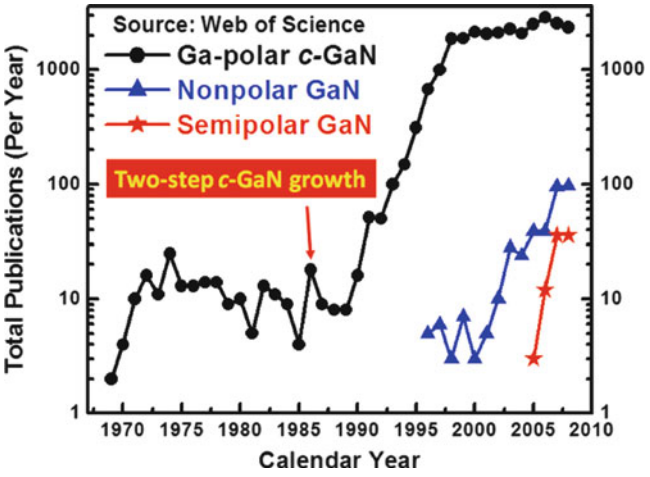

Fig. 1.1 A plot of the total publications per year for Ga-polar *c*-plane, nonpolar, and semipolar GaN, reflecting the research activities on the individual orientation. The *arrow* indicates the most crucial breakthrough in improving heteroepitaxial *c*-plane GaN material quality by a two-step growth scheme in the late 1980s [3]

on foreign substrates has been extensively investigated, motivated by the prospects of high-brightness displays and, more recently, energy-efficient illumination using InGaN-based light-emitting diodes (LEDs). The two major challenges in the field of InGaN-based LEDs are the "efficiency droop" under a high injection current density and the "green gap" in the plot of efficiency versus emission wavelength [4]. So far most of InGaN-based LEDs are built along Ga-polar (0001) orientation, which is susceptible to the strong internal electric field induced by the spontaneous and the piezoelectric polarization in Wurtzite III-nitrides. The pronounced tilting of the energy band edges of InGaN quantum wells (QWs) causes a spatial separation between electrons and holes in the QWs and hence reduces the internal quantum efficiency (IQE) of carrier recombination. This effect gets much more pronounced as the emission wavelength is steered from blue to green and yellow ranges due to the increased indium composition in the QWs, giving a great contribution to the well-known "green gap." The tilting of the band edges in the active region also narrows down the effective width of the QWs and hence increases the effective carrier density in the QWs, which favors Auger nonradiative recombination. Meanwhile, the effective barrier height is reduced by the tilting of the band edges, which can facilitate carrier leakage under an applied bias. Both Auger recombination and carrier leakage have been proposed as the likely mechanisms responsible for the universally observed "efficiency droop" phenomenon [5, 6]. To address these challenges, there have been concerted efforts in exploring III-Nitride materials and devices along nonpolar and semipolar crystallographic orientations [7–12]. Very promising reports of LEDs and laser diodes on nonpolar and semipolar GaN bulk substrates, in the longer wavelength of green and yellow, tend to validate the concept of crystallographic engineering [13–18]. The homoepitaxial nonpolar/semipolar

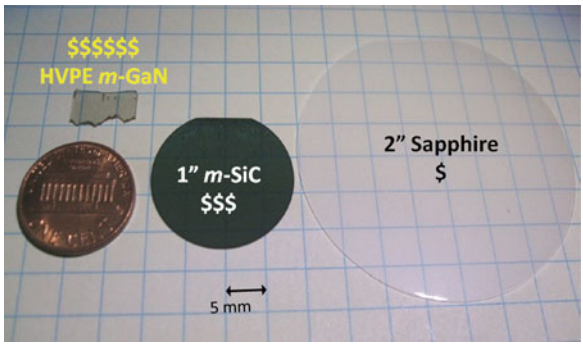

Fig. 1.2 A photo of 2-inch sapphire, 1-inch *m*-plane SiC, and nonpolar/semipolar GaN substrate with a typical size of 5 × 10 mm prepared by hydride vapor phase epitaxy (HVPE) [3]

LEDs are mitigating the "green gap" [19] and have also shown significantly reduced "efficiency droop" [20–23].

However, nonpolar and semipolar GaN bulk substrates are presently very small in size and expensive in price (Fig. 1.2), because they are sliced vertically and at an inclined angle, respectively, from a thick *c*-plane GaN substrate prepared by hydride vapor phase epitaxy (HVPE) [24]. Given the very limited availability of HVPE GaN wafers in the foreseeable future, it is likely that heteroepitaxy on large-area, cost-effective foreign substrates will remain the viable pathway for nonpolar and semipolar devices to reach the mass market. The research activities, including both homoepitaxy and heteroepitaxy, of nonpolar and semipolar GaN are gaining more and more momentum (Fig. 1.1). However, heteroepitaxy of nonpolar (*a*- and *m*-plane) and semipolar GaN is still explored empirically and disjointedly, often giving a poor morphology with surface striations and faceted pits, and a defective microstructure, including basal-plane stacking faults (BSFs) bounded by partial dislocations (PDs) [25–33].

In this chapter, we present kinetic Wulff plots (*v*-plots) as a novel and effective methodology to interpret the major challenges as well as their causes in the heteroepitaxy of nonpolar and semipolar GaN, and to control the heteroepitaxial dynamics on planar substrates with a rational design of multistep growth procedure. Orientation controlled epitaxy (OCE) on nonplanar substrates is introduced and experimentally confirmed as an innovative and promising approach to further boost the material quality of heteroepitaxial nonpolar and semipolar GaN films. The major research progresses in improving nonpolar and semipolar GaN material quality are summarized in a graphic presentation.

1.2 Kinetic Wulff Plot (*V*-Plot) of GaN

The standard two-step growth procedure of *c*-plane GaN does not work for nonpolar and semipolar GaN heteroepitaxy. The conventional approach widely taken by the III-Nitride community is to optimize the growth conditions through

knob-turning exercises, which normally takes a lot of time and efforts even just for one nonbasal orientation. This time-consuming cycle needs to be repeated for the GaN heteroepitaxy along every different nonbasal orientation. Here we adopted a nonconventional methodology, kinetic Wulff plot, a three-dimensional (3D) polar plot of the growth velocities (*v*-plots) along the polar, semipolar, and nonpolar orientations of GaN under various MOCVD growth conditions.

The study of shape evolution and growth velocity anisotropy for GaN to date has been largely empirical. Based on the observations of GaN epitaxial lateral overgrowth (ELOG), Hiramatsu et al. [34] compiled the trends of growth velocities for (0001), {10$\underline{1}$1}, and {11$\underline{2}$2} planes. Du et al. [35] proposed a 3D *v*-plot for GaN using the ratios of growth velocities from the same set of facets formed by selective area growth (SAG). Their study presented a conceptual framework correlating the 3D *v*-plot with the GaN SAG mesa shape evolution, though the information on the *v*-plot for nonpolar and the entire N-polar "hemisphere" was largely speculative. In the present work, we take into account the great asymmetry between the Ga-polar and the N-polar "hemispheres" that we have determined in the construction of the 3D *v*-plot and demonstrated that the full-range *v*-plot provides crucial insights to unlock the complex heteroepitaxial dynamics, especially at facetted growth fronts of opposite curvature nature. In the case of *convex* growth, such as island formation during the initial phase of heteroepitaxy, the fast-growing facets grow to extinction while the slow-growing facets expand and ultimately define the island shape (Fig. 1.3a); the crystallographic planes at the minima of a *v*-plot therefore dictate the initial evolution [35, 36]. On the other hand, the presence of *concave* growth fronts is a salient feature in the coalescence stage of heteroepitaxy, as edges of islands come into contact. During *concave* growth, fast-growing facets expand at the expense of slow-growing facets (Fig. 1.3a) and dominate the growth fronts [35, 36]. By employing an annular-ring mask pattern (Fig. 1.3b), we can form convex and concave planes concurrently through SAG. For example, a *c*-plane GaN SAG mesa (Fig. 1.3d) exhibits six {10$\underline{1}$1} planes on the outside, corresponding to the slow-growing convex planes, and six {11$\underline{2}$2} planes on the inside, corresponding to the fast-growing concave planes, together with the top (0001) [35]. More complicated faceting morphology is exhibited during nonpolar *a*-plane (11$\underline{2}$0) (Fig. 1.3e) and semipolar (11$\underline{2}$2) GaN SAG (Fig. 1.3f) due to their reduced symmetry (Fig. 1.3c).

Consecutive SAG experiments [36] were employed to monitor the differential advances of both the convex and the concave facets, which gave a direct measure of the relative growth velocities for those orientations. Appropriate trigonometric interpretations were used to bridge the experimental data points for the construct of GaN *v*-plots. Figure 1.4a shows a 3D *v*-plot of GaN, viewed along the surface normal of (10$\underline{1}$1), for a growth condition of 1, 070°C, 100 mbar, and a V/III ratio of 250. False-colored shading from red to blue is used to depict the measured (or interpolated) growth velocities. We have identified cusp points (local minima) at (0001), {10$\underline{1}$1}, {11$\underline{2}$0}, {10$\underline{1}$0}, and (000$\underline{1}$). These facets are responsible for defining the shape of nucleation islands having a convex curvature on a mesoscopic scale. In addition to plotting the cusps in Fig. 1.4a, we have also included the

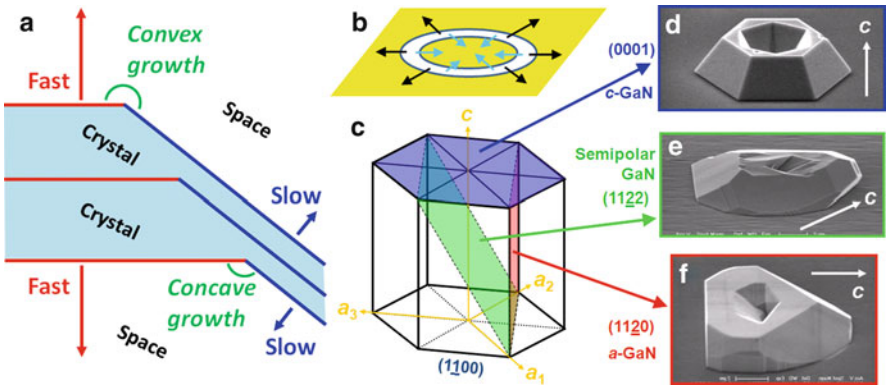

Fig. 1.3 (**a**) Schematic diagram showing the principle of morphological evolution for convex (toward the upper right) and concave (toward the lower left) growth fronts. The convex growth front will be dominated by the slow-growing facets while the concave growth front by the fast-growing facets. (**b**) Schematic of an annular ring opening, which produces both inward concave and outward convex growth fronts. (**c**) Schematic hexagonal lattice showing the *c*-plane (0001), nonpolar *a*-plane (11$\bar{2}$0), and semipolar (11$\bar{2}$2). SEM images of GaN SAG mesas grown out of an annular ring opening on (**d**) *c*-plane (0001), (**e**) semipolar (11$\bar{2}$2), and (**f**) nonpolar *a*-plane (11$\bar{2}$0) GaN surfaces

measured saddle points (i.e., a local minimum along one direction, but a local maximum along the orthogonal direction) determined by the concave growth fronts in the inner ring.

Given the different atomic bonding configurations on each plane [34], it is expected that the growth velocities and the 3D *v*-plot depend strongly on the local stoichiometry of reactants. This is confirmed by another set of differential SAG experiments under a condition of much higher V/III ratio ~1,700 and higher reactor pressure 300 mbar. In this case, the relative growth velocities of nearly all the Ga-polar planes (the northern "hemisphere") are suppressed (Fig. 1.4f) while the equatorial portion of the *v*-plot pertaining to the nonpolar *a*-planes {11$\bar{2}$0} is increased considerably. These *v*-plots can be considered "finger prints" of a specific growth condition or procedure (e.g., flow modulation, co-doping, etc.) that can provide insights to a wide range of observed morphology with cross-platform insensitivity.

As discussed earlier, the minima on a 3D *v*-plot determine the shape evolution during the convex growth (Fig. 1.3a), manifested in the formation of islands bound by the cusp planes (Fig. 1.3d–f). The coalescence stage, in contrast, is governed by the less-understood concave growth when neighboring islands (with convex facets) come into contact. Coalescence produces a growth front that is concave along only *one* of the two spherical axes (azimuth, for instance) while remaining convex along the other orthogonal spherical axis (polar, for instance). The dominant planes during coalescence therefore correspond to saddle points [35, 36] in the *v*-plots, rather than maxima as one might suppose. The important saddle points are {11$\bar{2}$2} in the

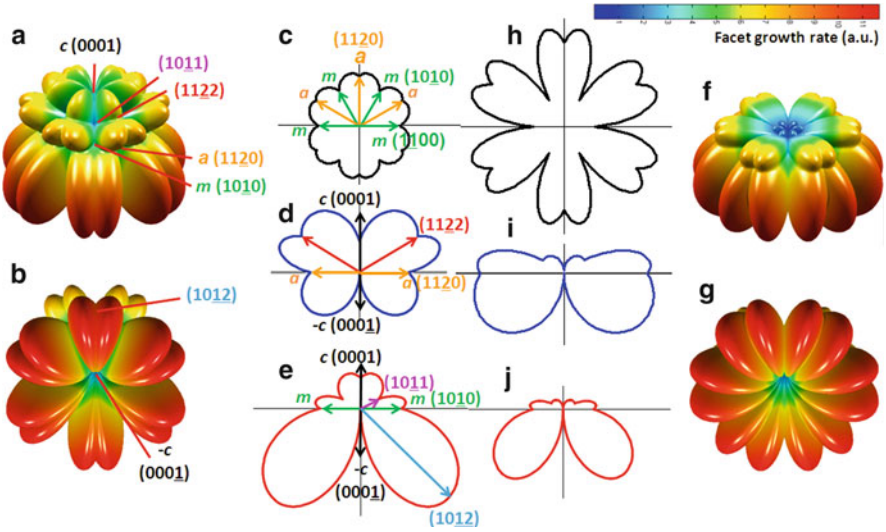

Fig. 1.4 Kinetic Wulff plots (v-plots) for a low reactor pressure and low V/III ratio condition [(**a**)–(**e**)] and a high reactor pressure and high V/III ratio condition [(**f**)–(**j**)]. For the 3D v-plots, the [0001] axis is set as $\theta = 0°$, and the m-axis as $(\theta, \varphi) = (90°,\ 0°)$. The Ga-polar hemisphere [(**a**) and (**f**)] and the N-polar hemisphere [(**b**) and (**g**)] 3D v-plots are viewed at an angle of $(62°,\ 0°)$ and $(150°,\ 0°)$, respectively. (**c**) and (**h**) are the 2D v-plots for the prism planes mapped onto the basal c-plane; (**d**) and (**i**) the 2D v-plots for the orientations within the m-plane; (**e**) and (**j**) the 2D v-plots for the orientations within the a-plane. Note that a sixfold symmetry is assumed for all the v-plots and the symmetry reduction due to the mask effect during SAG is ignored in this chapter for simplicity

Ga-polar hemisphere (Fig. 1.4a) and {10$\underline{1}$2} in the N-polar hemisphere (Fig. 1.4b). Planes associated with these saddles points are of particular importance in the coalescence stage of nonpolar and semipolar GaN heteroepitaxy to the final surface morphology and the microstructural quality, as will be discussed in detail later.

1.3 Heteroepitaxy of Nonpolar GaN on Planar Substrates

Nonpolar GaN can be epitaxially grown on various foreign substrates, including a-/m-plane SiC [25, 28, 29, 37], (100) $LiAlO_2$ [38–40], r-plane sapphire [26, 27, 30, 41–44], etc. SiC substrates are very expensive and not widely available, especially for nonpolar orientations. (100) $LiAlO_2$ has a small lattice mismatch with nonpolar m-plane GaN, but a poor thermal and chemical stability [45]. In contrast, r-plane sapphire is the most commercially available cost-effective substrates with a good thermal and chemical stability, and hence is widely used for the growth of nonpolar (11$\underline{2}$0) a-plane GaN (a-GaN).

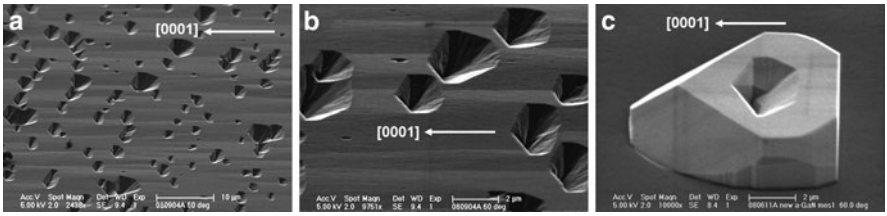

Fig. 1.5 SEM perspective view of nonpolar (11$\underline{2}$0) $a-$ GaN film (**a**) and (**b**), showing a high density of faceted pits and striations, and an SAG $a-$ GaN mesa (grown out of an annular ring opening) with a concave void (**c**). The faceted pits on the $a-$ GaN film surface resemble very much to the concave void of the $a-$ GaN SAG mesa

In the heteroepitaxy of nonpolar a-GaN, there are two major challenges, poor surface morphology and defective microstructure. On the surface of heteroepitaxial a-GaN film, there are often triangular/pentagonal faceted pits and striations along the in-plane c-axis [0001] [27], as shown in Fig. 1.5a, b. The faceted surface pits resemble very much to the concave void of the $a-$GaN SAG mesa (Fig. 1.5c) grown out of an annular ring opening (Fig. 1.3b) [36], indicating that the faceted surface pits are due to incomplete coalescence. To eliminate the surface pits, the vertical out-of-plane a-axis growth needs to be slowed down and the lateral in-plane growth rates be enhanced, which are favored by growth conditions of a low V/III ratio and a low reactor pressure according to the v-plots [36, 42]. The a-GaN surface striations consist of facets vicinal to the surface (11$\underline{2}$0) (Fig. 1.5a, b). The growth rates of the vicinal facets are comparable to that of the vertical a-axis growth under a low V/III and a low reactor pressure, and therefore the striations persist on the surface even after a long growth. A change in growth conditions to enlarge the difference in growth rate between the vicinal facets and the (11$\underline{2}$0) surface has been found effective in relieving the pronounced striations [42].

The other challenge in a-GaN heteroepitaxy on r-plane sapphire lies in their dissimilar structure, including the in-plane stacking mismatch and the lattice mismatch (16 and 1.3% along the m- and c-axes of GaN, respectively), which lead to a high density of microstructural defects, including BSFs bounded by PDs with a typical density of 10^5–$10^6\,\mathrm{cm}^{-1}$ and 10^{10}–$10^{11}\,\mathrm{cm}^{-2}$, respectively [46]. These extended defects propagate along the growth axis usually throughout the nonpolar GaN film (Fig. 1.6b), and hence deteriorate material quality and device performance. It has been observed by various groups that BSFs and associated PDs are nucleated at the interface of nonpolar GaN with the underlying template (Fig. 1.6b) [28, 29, 37, 46]. During the initial growth of nonpolar/semipolar GaN on a *heterogeneous* template (foreign substrates, AlN buffer [29, 37], SiO_2 [33, 47–49], etc.), rough surface morphology [38, 39], atomic (partial) steps [40], and/or impurities on the surface of the underlying template may trigger nucleation errors at the cubic sites, especially for the N-face lateral growth. BSFs may also be formed during the coalescence of nonpolar GaN islands whose basal-plane stacking sequences are out of registry [33]. I_1 BSFs having a displacement vector with a

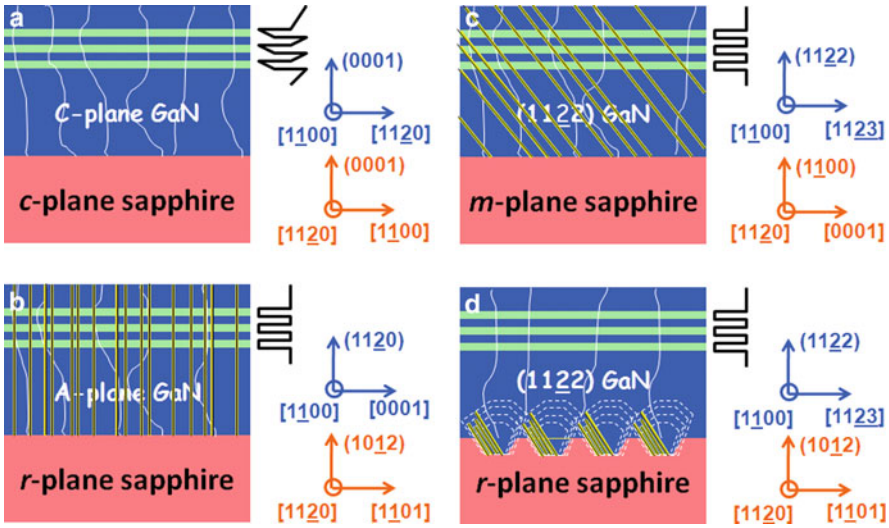

Fig. 1.6 Schematic LED structures build on (**a**) *c*-plane GaN/*c*-plane sapphire, (**b**) nonpolar *a*-plane GaN/*r*-plane sapphire, (**c**) semipolar (11$\underline{2}$2) GaN/*m*-plane sapphire, and (**d**) semipolar (11$\underline{2}$2) GaN/patterned *r*-plane sapphire. Perfect threading dislocations are represented by *white curved lines*. BSFs and their associated PDs are indicated by *yellow* and *black straight lines*. An energy diagram drawing is shown on the right side of InGaN MQWs (in *green*) for each structure

c-axis component can contribute to strain relaxation [39, 50, 51]. One effective way to reduce the formation of BSFs in nonpolar GaN due to strain relaxation is to introduce composition-graded AlGaN layers between the AlN buffer and the GaN films [37].

In the study of *c*-plane GaN (*c*-GaN) growth, a 3D to 2D transition (a roughening-recovery process) was found crucial in achieving improved crystalline quality [52]. Based on the *v*-plots (Fig. 1.4), we designed a two-step growth procedure (beyond the initial buffer layer) for *a*-GaN with different V/III ratios and reactor pressure to effectively reduce the defect density [41–43].

In this study, all the *a*-GaN samples were grown at 1, 050°C with an AlN buffer (deposited at 1, 150°C) on nominally on-axis *r*-plane sapphire in an Aixtron horizontal MOCVD reactor. Trimethylgallium (TMGa), trimethylaluminium (TMAl), and ammonia (NH_3) were used as the precursors for Ga, Al, and N, respectively. Hydrogen was used as the carrier gas if not specified separately. For the baseline (sample A), 2 − μm-thick *a*-GaN was directly grown on the AlN buffer at 1, 050°C, a reactor pressure, P, of 60 mbar and a V/III ratio of 187. For all other samples (B-F) a 3D-growth stage was introduced with various P and V/III (Table 1.1) to control the growth dynamics, before returning to the baseline condition. Sample F, having the longest roughening growth stage, was grown nominally twice as thick as other samples to ensure a fully coalesced pit-free surface.

Table 1.1 Growth parameters and characterization results of nonpolar *a*-GaN samples A–F

Sample	First-step *a*-GaN			*c*-axis LCL (nm)	BSF density $\times 10^5\, cm^{-1}$
	V/III	*P*(mbar)	*t*(min)		
A	/	/	0	19	5.3
B	1,440	60	10	24.5	4.1
C	2,162	100	17	30.4	3.3
D	2,162	200	17	36.5	2.7
E	1,682	300	17	45.4	2.2
F (F4)	1,682	300	40	60	1.7

For sample A (one-step growth), the in situ reflectance trace exhibits instant oscillations (Fig. 1.7a) indicating a quasi-2D growth mode. According to the kinetic Wulff plots [36, 42], the vertical growth can be greatly enhanced while the lateral growth (especially along the *c*-axis) is slowed down under an increased V/III ratio and/or an elevated P, thus facilitating the formation of *a*-GaN islands with a "tall" aspect ratio. During the first-step growth of samples B–F, as the V/III ratio and/or P increase, surface becomes increasingly rough as revealed by the progressive decay of the reflectance traces, eventually down to nearly background (Fig. 1.7b–f). Once the growth is switched back to the baseline condition (for the second-step growth), island coalescence through lateral growth occurs at a rate that is inversely correlated with the extent of roughening after the first-step growth. The amplitude of reflectance oscillations decreases from sample A to F because of their increased surface striations, which can be relieved by an additional third-step growth [42].

The microstructural extended defects in *a*-GaN films (Fig. 1.6b) are much more complicated than those in *c*-GaN due to the reduced symmetry [41, 42]. *A*-GaN may contain not only $a-$, $c-$, and $a+c$ type dislocations with a Burgers vector (BV) of $1/3 < 11\underline{2}0 >$, $< 0001 >$, and $1/3 < 11\underline{2}3 >$, respectively, but also planar defects including BSFs and prismatic-plane stacking faults (PSFs). I_1, I_2, and E type BSFs are normally bounded by Frank–Shockley, Shockley, and Frank PDs with a BV of $1/6 < 20\underline{2}3 >$, $1/3 < 10\underline{1}0 >$, and $1/2 < 0001 >$, respectively [46]. Given the complexity of TDs/PDs, it is necessary to measure X-ray rocking curves (XRCs) for both on- and *off-axes* planes over a sufficiently large azimuthal and polar angular space (Fig. 1.8a, b) to obtain a comprehensive knowledge of the microstructure of *a*-GaN [41, 42]. The full widths at half maximum (FWHMs) were obtained through fitting with pseudo-Voigt functions. It is worthy to review the visibility criteria for stacking faults and dislocations under X-ray diffraction. For an XRC with a diffraction vector $\boldsymbol{g}$ to be broadened by a stacking fault with a displacement vector $\boldsymbol{R}$, the $\boldsymbol{g} \cdot \boldsymbol{R}$ product must be a *noninteger* and the stacking axis has a substantial component along the X-ray rocking direction [42]. A dislocation with a Burgers vector $\boldsymbol{b}$ can broaden an XRC with a diffraction vector $\boldsymbol{g}$, if the $\boldsymbol{g} \cdot \boldsymbol{b}$ product is *nonzero* (including integers) [42].

Figure 1.8c shows the FWHM of the on-axis $(11\underline{2}0)$ XRCs as a function of the azimuthal angle, φ. The baseline sample A (one-step growth with instant reflectance oscillations) exhibits very anisotropic FWHMs for the on-axis $(11\underline{2}0)$ XRCs, similar

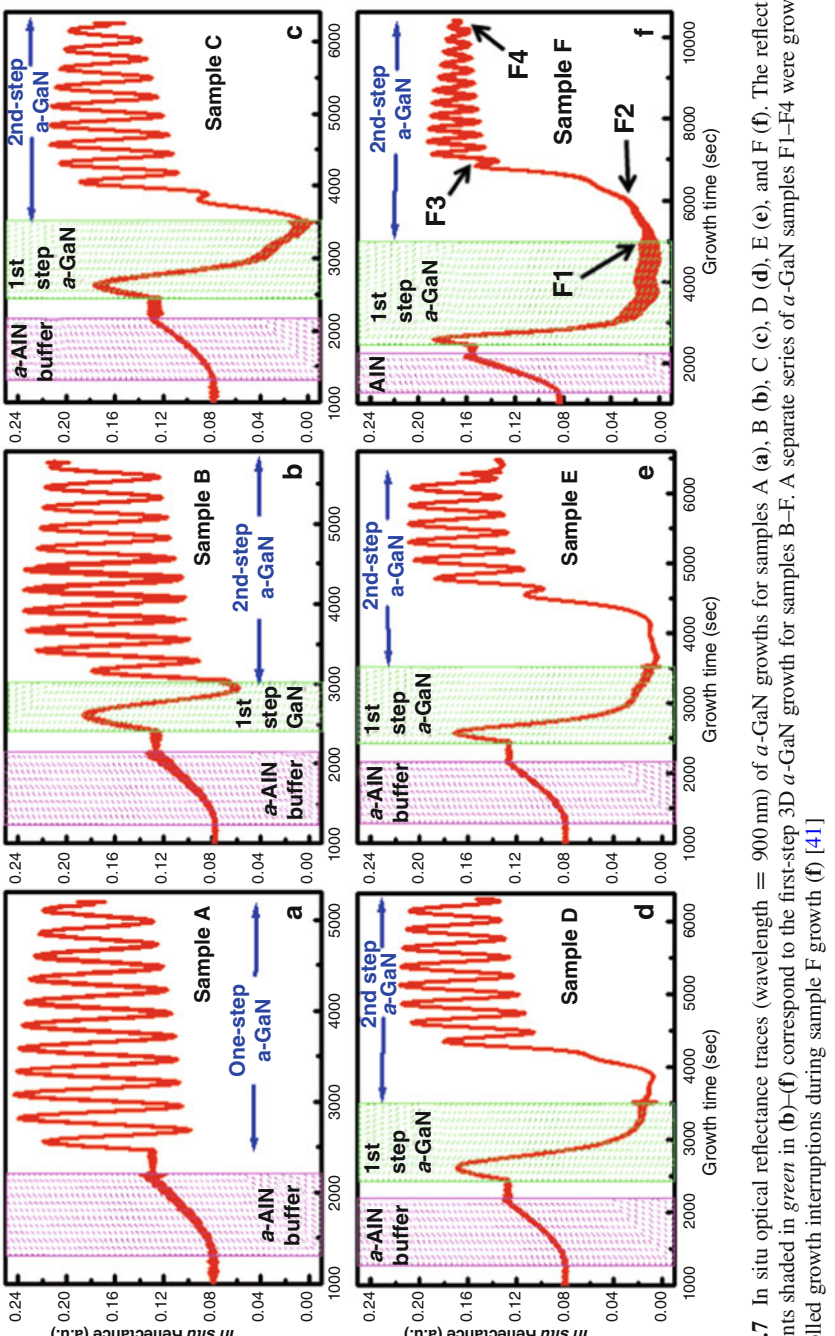

Fig. 1.7 In situ optical reflectance traces (wavelength = 900 nm) of *a*-GaN growths for samples A (**a**), B (**b**), C (**c**), D (**d**), E (**e**), and F (**f**). The reflectance segments shaded in *green* in (**b**)–(**f**) correspond to the first-step 3D *a*-GaN growth for samples B–F. A separate series of *a*-GaN samples F1–F4 were grown by controlled growth interruptions during sample F growth (**f**) [41]

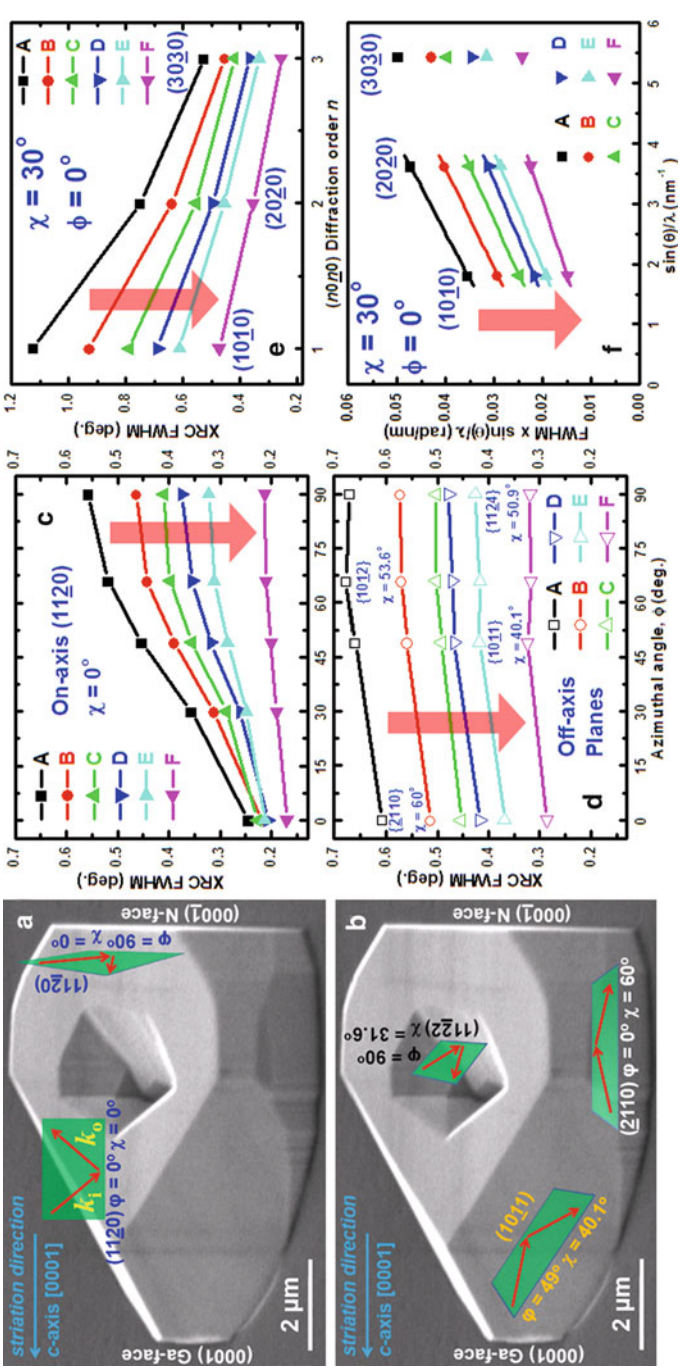

Fig. 1.8 SEM image of an *a*-GaN SAG mesa for the illustration of (**a**) on-axis and (**b**) off-axis XRC configurations. For $\varphi = 0$ and 90°, the X-ray rocking direction is parallel and perpendicular to the *c*-axis [0001], respectively. The incident and diffracted X-ray beams (*red arrows*) rock within a plane (shaded in *green*) for each diffraction plane with its index and orientation labeled in the vicinity. The (**a**) on-axis (11$\bar{2}$0) ($\chi = 0°$) and (**b**) off-axis planes ($\chi \neq 0°$), such as (10$\bar{1}$1), ($\bar{2}$110), (30$\bar{3}$0), and (11$\bar{2}$2), were measured in symmetric and skew symmetric geometries, respectively. The FWHM of the (**c**) on-axis and (**d**) off-axis XRCs of *a*-GaN as a function of the azimuthal angle, φ. (**e**) The FWHMs of *m*-plane ($n0\bar{n}0$) XRCs ($n = 1, 2$, and 3; $\varphi = 0°$, $\chi = 30°$); (**f**) the modified WH plots. The *straight lines* in (**f**) are the linear fits to the (10$\bar{1}$0) and (20$\bar{2}$0) data points of each *a*-GaN sample [41]

to many previous reports. However, with the introduction of a 3D growth stage, the FWHM of the on-axis (11$\underline{2}$0) XRC at $\varphi = 90°$ decreases monotonically from sample A to F, and the FWHM-φ plots become less steep, indicative of improved isotropy. Given the insensitivity of (11$\underline{2}$0) diffraction to BSFs, the anisotropic broadening of the on-axis (11$\underline{2}$0) XRCs may be caused by the anisotropy in mosaic tilt and/or domain size, as well as the PSFs within the inclined a-planes with a displacement vector of $1/2 < 10\underline{1}1 >$. Mosaic twist (in-plane misalignment) is another important aspect of the microstructure and normally correlated with dislocations with an edge component. To study twist in the a-GaN films, XRC measurements were implemented in a *skew* symmetric geometry for *off-axis* planes having an inclination angle χ with respect to the on-axis (11$\underline{2}$0) at various azimuths (Fig. 1.8b). As shown in Fig. 1.8d, for all the samples the FWHM-φ plots of the off-axis XRCs are fairly flat with a small anisotropy [unlike the case of on-axis XRCs in Fig. 1.8c), implying a uniform angular distribution of dislocations with an edge component. For sample A, the off-axis XRC FWHMs are very high, ranging from 0.6 to 0.7°. With the insertion of 3D island growths, the off-axis XRC FWHMs decrease *evenly* for all the azimuths from samples B to F, reaching a ~50% reduction for the case with a prolonged 3D growth.

By treating BSFs as boundaries between incoherently scattering domains [53], we can determine the lateral coherence length (LCL) along the c-axis and estimate the BSF density in nonpolar a-GaN film through a modified Williamson-Hall (WH) analysis [41,42] on m-plane ($n0\underline{n}0$) diffraction ($n = 1$, 2, and 3; $\varphi = 0°$, $\chi = 30°$) in a skew symmetric geometry with the X-ray rocking along the c-axis (Fig. 1.8b). The XRC FWHMs for all three diffractions decrease monotonically from sample A to F (Fig. 1.8e), another indicator of the clear trend of improved structural quality. It is noted that for all the samples, the FWHMs of (10$\underline{1}$0) and (20$\underline{2}$0) XRCs are much broader than that of (30$\underline{3}$0) XRC, because the former two XRCs are predominantly broadened by the short c-axis LCLs due to the presence of BSFs, which is more clearly revealed by the WH plots in Fig. 1.8f. Since (30$\underline{3}$0) diffraction is insensitive to the presence of BSFs, the (30$\underline{3}$0) data points in the WH plots (Fig. 1.8f) are significantly lower than the expected values from the linear fits to the corresponding (10$\underline{1}$0) and (20$\underline{2}$0) data points of each sample. The c-axis LCLs can be derived from the y-axis intercepts (y_o) of the linear fits, LCL $= 0.9/(2y_o)$. And the reciprocal of the LCLs gives the density of BSFs. The determined LCL and BSF density of all the samples are summarized in Table 1.1. It is clearly shown that the more the 3D process is involved in the first-step growth, the longer the c-axis LCL and the lower the BSF density (~70% reduction).

To verify the substantial reduction in the densities of both BSFs and dislocations, we examined the microstructure of a-GaN samples A and F by transmission electron microscopy (TEM) images taken from three orthogonal axes, including plan-views (Fig. 1.9a, b, e, f), and two cross-section views along the in-plane c- (Fig. 1.9c, g) and m-axes (Fig. 1.9d, h). Most of the observed BSFs were of I_1 type, normally bounded by Frank–Shockley PDs ($\boldsymbol{b} = 1/6 < 2\underline{2}03 >$). The dislocations observed in the plan-view were all partials according to the one-to-one location correlation between the ends of the BSFs in Fig. 1.9e and the PDs in Fig. 1.9f. No perfect

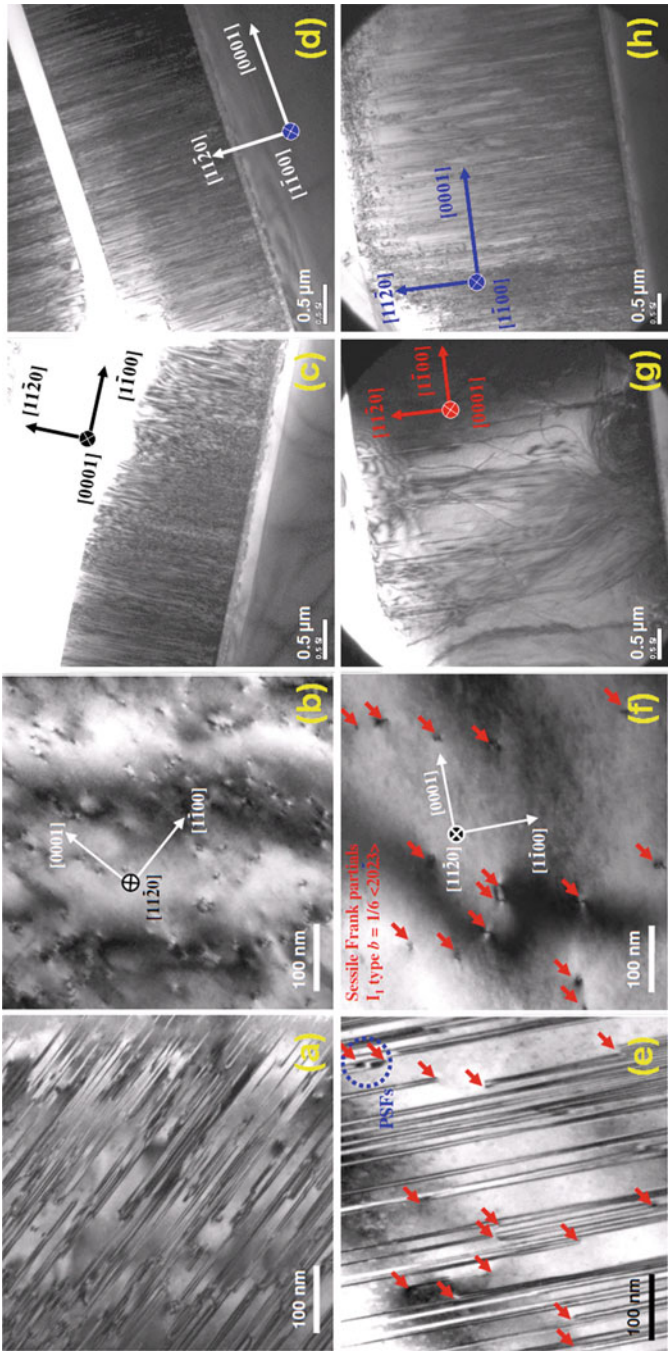

Fig. 1.9 Plan-view TEM images of the one-step grown [(**a**) and (**b**)] and the two-step grown [(**e**) and (**f**)] nonpolar *a*-plane GaN samples. The **g** vectors were $1\underline{1}00$ for (**a**) and (**e**), and 0002 for (**b**) and (**f**), to reveal the SFs and the PDs, respectively. The Frank–Shockley PDs ($b = 1/6 < 20\underline{2}3 >$) are indicated by the *red arrows*. The PSFs observed on the surface of the two-step grown *a*-plane GaN sample are *circled* in (**e**). Cross-section TEM images of the one-step grown [(**c**) and (**d**)] and the two-step grown *a*-GaN samples [(**g**) and (**h**)]. (**c**) and (**g**) were taken near the [0001] axis with $\mathbf{g} = 1\underline{1}00$. (**d**) and (**h**) were taken near the [$1\underline{1}00$] axis with $\mathbf{g} = 11\underline{2}0$ [42]

dislocations were observed in the view although the diffraction configurations adopted in this study did satisfy the visibility criteria for perfect dislocations. As revealed in Fig. 1.9b, f, the PD density of sample F ($\sim 6 \times 10^9\,\mathrm{cm}^{-2}$) was much lower than that of sample A ($\sim 5 \times 10^{10}\,\mathrm{cm}^{-2}$), which was consistent with the 2–3 times difference in the XRC FWHMs between the two samples (Fig. 1.8). By calculating the total length of the observed BSFs divided by the image area, we estimated the BSF density in the *a*-GaN films to be $\sim 1 \times 10^6$ and $\sim 4 \times 10^5\,\mathrm{cm}^{-1}$ for samples A (Fig. 1.9a) and F (Fig. 1.9e), respectively. The differences between the TEM measurement and the XRC WH analysis can be accounted for by their different nature and principles [42]. But both the methods confirmed the efficacy of the two-step growth process in significantly reducing the BSF density (60–70%).

To unveil the possible mechanisms for the density reduction of BSFs and PDs, controlled growth interruptions [42] were carried out during two-step growth of sample F, giving a series of samples F1–F4 (Fig. 1.7f). Scanning electron microscope (SEM) was utilized to observe the morphological evolution. Sample F1 presented a very rough surface consisting of tall mesas separated by big voids, within which there were many ridge-like islands (roughly aligned along the *c*-axis) (Fig. 1.10a). After 20 min into the second-step growth (sample F2), the flat top area of the GaN mesas substantially increased, and the previous big voids were largely filled (through concave growths), leaving behind chains of pits along the *c*-axis (Fig. 1.10b). During the following 17.5-min growth (sample F3), the chains of pits were zipped up by lateral concave growth, producing many striations (Fig. 1.10c). For sample F4, a 90-min growth under the second-step condition fully eliminated the pits (Fig. 1.10d).

A correlation study [42] between the morphological evolution and microstructure development has revealed that Frank–Shockley PDs are strictly confined within the basal plane, because it is energetically unlikely to bend a planar defect BSF out of the basal plane, and the BSFs and the associated PDs projected along the in-plane *m*-axis are always straight vertical lines (Fig. 1.9d, h). But the PDs can be bent by the inclined $\{10\underline{1}1\}$ and the vertical $\{10\underline{1}0\}$ growth fronts (Figs. 1.10a and 1.11c) toward the *m*-axis (Figs. 1.9g and 1.11a) [42], which greatly cut down the density of threading PDs while significantly extending the dimension of BSFs on the surface (Figs. 1.9e and 1.11a). For the two-step grown *a*-GaN sample F, the increased spacing between the BSFs in the plan-view TEM image (Fig. 1.9e) and the reduced density of the vertical lines in the cross-section TEM image along the in-plane *m*-axis (Fig. 1.9h), together with the knowledge of the *v*-plots, provided the rational bases of our model for the BSF reduction through the two-step growth process. The first-step growth of *a*-GaN produces tall convex mesas separated by tiny, incipient ridge-like islands (Figs. 1.10a and 1.11c) containing many BSFs. Coalescence of those tall mesas results in concave growth fronts along $[000\underline{1}]$, with four of the six $\{10\underline{1}2\}$ facets forming an overhanging structure next to the incipient islands (Figs. 1.10a and 1.11c). These *fast-growing* $\{10\underline{1}2\}$ facets advance and sweep laterally along $[000\underline{1}]$ over the incipient islands, burying and blocking the vertical propagation of BSFs as depicted in Fig. 1.11a, b [42]. Our model of BSF and PD reduction has been supported by the one-to-one location correlation

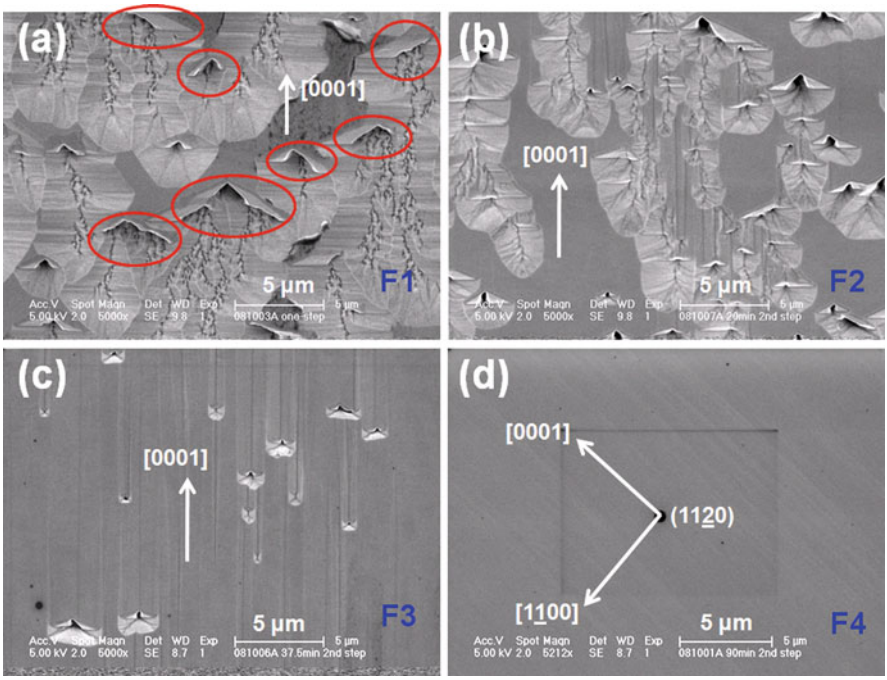

Fig. 1.10 SEM surface images of samples F1–F4 (Fig. 1.7f) showing the evolution of the nonpolar *a*-GaN surface morphology during the two-step growth process. The *red circles* in (**a**) marked out regions showing lateral growth of big mesas along [000$\bar{1}$] over the neighboring small islands [42]

between SEM (Fig. 1.11c) and monochromatic cathodoluminescence (CL) images (Fig. 1.11d) of the same area of *a*-GaN sample F1. Most of the CL emission came from the regions "behind" the over-hanging {10$\bar{1}$2} growth fronts circled by the dash lines, indicating a good material quality with few defects.

1.4 Heteroepitaxy of Semipolar GaN on Planar Substrates

M-plane sapphire (*m*-sapphire) is widely used for semipolar GaN growth, but can produce both nonpolar (10$\bar{1}$0) *m*-GaN and two kinds of semipolar orientations, (11$\bar{2}$2) and (10$\bar{1}$3) [32, 54, 55]. When *m*-sapphire surface is not thoroughly nitridized, the as-grown GaN surface often consists of both (11$\bar{2}$2) orientation and (10$\bar{1}$3) twinned grains (Fig. 1.12). And the grain boundaries prohibited a complete coalescence. *M*-sapphire nitridation is found very effective to suppress the formation of mixed phase (10$\bar{1}$3) grains [32, 54] and consistently obtain (11$\bar{2}$2) GaN [55, 56]. Nitridation breaks the surface symmetry of *m*-sapphire [55] and favors the nucleation of (11$\bar{2}$2) orientation with N-polarity [34]. The

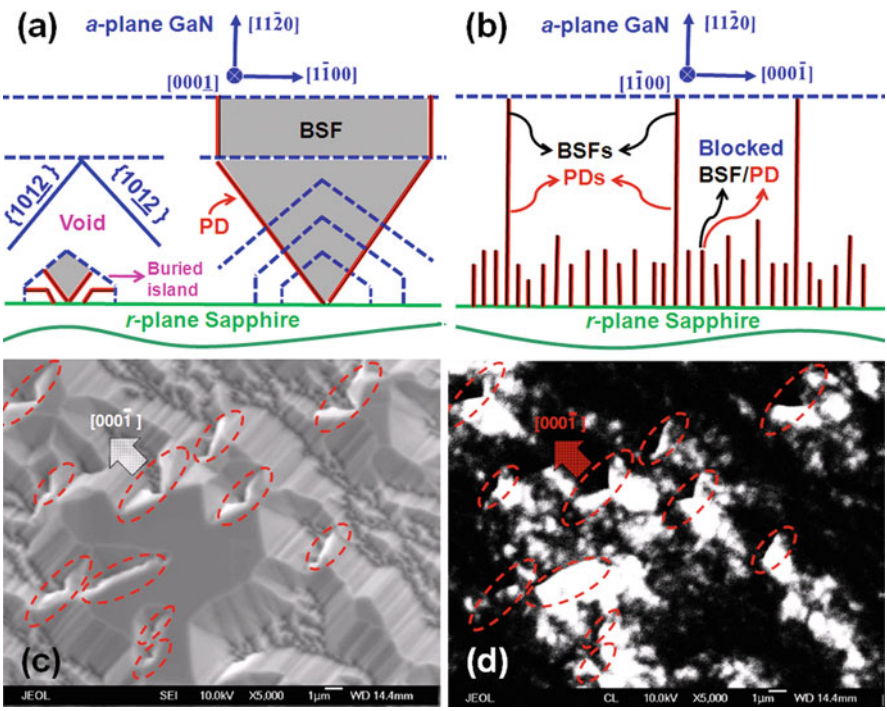

Fig. 1.11 Schematic model of the BSF blocking and the PD bending during the two-step growth of nonpolar *a*-plane GaN, cross-section viewed along the *c*-axis [0001] (**a**) and the *m*-axis [1$\underline{1}$00] (**b**). The *blue dashed lines* represent the *a*-plane GaN growth fronts, and the *red solid lines* are the PDs. BSFs are shown as the *shaded area* in (**a**) and the *straight black lines* in (**b**). The *vertical black lines* overlap with the *red lines* in (**b**), indicating that most of the BSFs are bounded by PDs. [42] SEM (**c**) and monochromatic (363 nm) CL image (**d**) of the same surface area of sample F1 *a*-plane GaN islands with the growth intentionally stopped at the end of the first-step roughening stage. The {10$\underline{1}$2} overhanging lateral overgrowth fronts toward the [000$\underline{1}$] circled in (**c**) show a good position correlation with most of the emitting regions (with a low defect density) in (**d**)

in-plane epitaxial relationships between (11$\underline{2}$2) GaN and *m*-sapphire (Fig. 1.6c) are $[1\underline{1}00]_{GaN}||[11\underline{2}0]_{sapphire}$ and $[\underline{1}\underline{1}23]_{GaN}||[0001]_{sapphire}$ with a lattice mismatch of 16.1 and −6.3%, respectively. Semipolar (11$\underline{2}$2) GaN heteroepitaxy shares the same challenge as nonpolar GaN, i.e., the high density of structural defects. Although BSFs and their bounding PDs confined within the basal plane are inclined to the (11$\underline{2}$2) surface by 58.4° (Fig. 1.6c) [33], they can still penetrate the entire semipolar GaN film and affect the material quality and device performance.

The study of semipolar (11$\underline{2}$2) GaN growth on nitridized *m*-sapphire was not carried out in an empirical manner by turning the knobs for the optimization of growth parameters. Instead, with the knowledge of the *v*-plots, we designed a two-step growth procedure for (11$\underline{2}$2) GaN to improve the material quality [56], similar to that for nonpolar *a*-GaN [41,42]. The two-step growth procedure for (11$\underline{2}$2) GaN

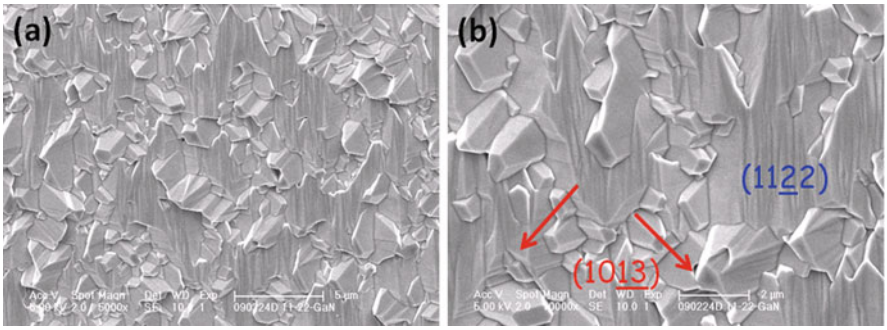

Fig. 1.12 SEM images of a semipolar (11$\underline{2}$2) GaN surface with many grains of mixed phase (10$\underline{1}$3) micro-twins due to insufficient nitridation of the *m*-plane sapphire substrate. The *arrows* indicate the *c*-axis direction of the (10$\underline{1}$3) micro-twins

Table 1.2 Growth parameters of semipolar (11–22) GaN samples S1–S4

Sample	The first-step GaN		The second-step GaN	
	P(mbar)	*t*(min)	*P*(mbar)	*t*(min)
S1	/	/	60	27
S2	200	5	60	22
S3	300	5	60	45
S4	300	15	60	60

involves a roughening-recovery process to actively induce dislocation bending and BSF blocking [42]. All the semipolar (11$\underline{2}$2) GaN samples were grown on nominally on-axis *m*-plane sapphire substrates which were nitridized during the temperature ramping up to 1,050°C in a mixture of NH_3 and N_2. In our previous report, we used a high-temperature AlN buffer for the growth of smooth (11$\underline{2}$2) GaN [56]. Here we show that a low-temperature (LT) GaN buffer (deposited at 600°C) can also give mirror-like (11$\underline{2}$2) GaN. After a thermal annealing of the LT-GaN buffer, (11$\underline{2}$2) GaN was grown at 1,000°C with 2 SLM NH_3 and 119 μmol/min TMGa. The difference in the growth parameters for samples S1–S4 is summarized in Table 1.2.

It should be pointed out the annealing behavior of the semipolar LT-GaN buffer is very different from that of the Ga-polar *c*-plane LT-GaN buffer [52]. As shown in Fig. 1.13, it took much longer time to anneal a semipolar LT-GaN buffer and get the in situ optical reflectance back close to the background level, and no "nose-like" peak was ever observed throughout the annealing process. For sample S1, the HT-GaN layer was grown under the one-step condition with instant oscillations (Fig. 1.13a) reflecting a quasi-two-dimensional (quasi-2D) growth mode. As we increased the reactor pressure from 60 to 200 mbar for the initial HT-GaN growth of sample S2, the reflectance began to decay in both average and amplitude from the very beginning (Fig. 1.13b), an indicator of 3D islanding growth. Once the growth condition was switched back the second-step condition (sample S1 condition), the reflectance was gradually recovered to sustained 2D oscillations. The final

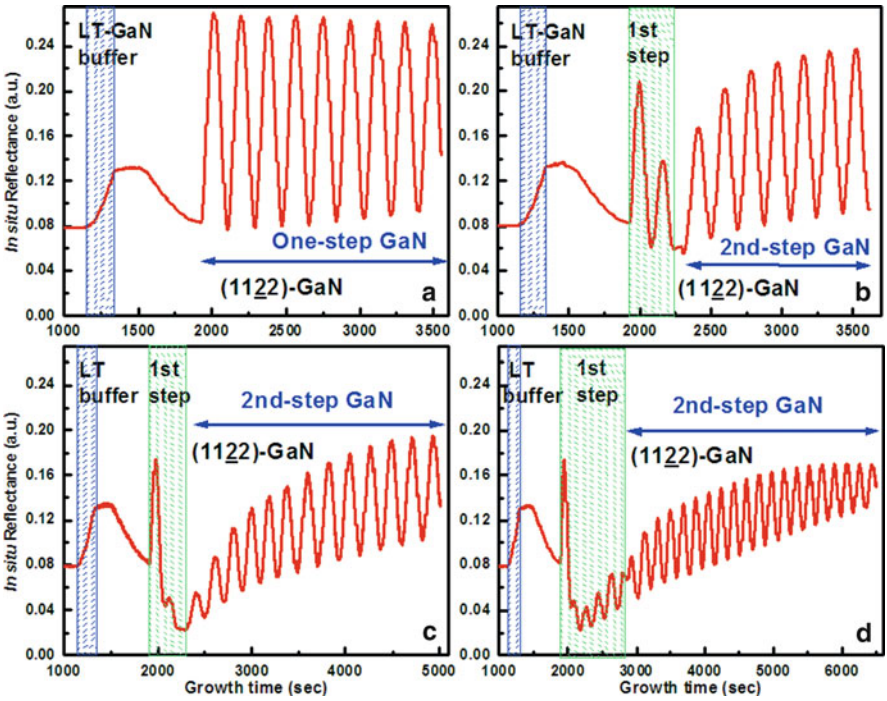

Fig. 1.13 In situ optical reflectance traces (wavelength = 550 nm) of semipolar (11$\underline{2}$2) GaN samples S1 (**a**), S2 (**b**), S3 (**c**), and S4 (**d**). The reflectance segments shaded in *green* in (**b**)–(**d**) correspond to the first-step 3D GaN growth for samples S2–S4

reflectance average for sample S2 was lower than that of sample S1 because of the striations on the sample S2 surface that were clearly observed under Nomarski optical microscope (not shown). From sample S2 to S3, we further elevated the reactor pressure to 300 mbar for the first-step GaN growth, the reflectance trace decayed in a faster pace to a lower level within the same growth time, and the recovery of the reflectance was accordingly much slower (Fig. 1.13c). For sample S4, the first-step growth time was increased to examine the effect of prolonged island growth (Fig. 1.13d). It is speculated that the difficulty in achieving a rapid recovery of the (11$\underline{2}$2) growth surface when it is very rough is because (11$\underline{2}$2) is a saddle point in the *v*-plots (Fig. 1.4a), a local minimum along the polar axis but a local maximum within the basal plane [36, 42].

Similar to the case of nonpolar GaN, the configuration of the planar and line defects in (11$\underline{2}$2) GaN is also quite complicated (Fig. 1.6c) [56]. To obtain a comprehensive knowledge of the microstructure, we also measured XRCs for both on-axis and *off-axis* diffraction planes (Fig. 1.14a, b). Figure 1.14c shows the FWHM of the on-axis (11$\underline{2}$2) XRCs as a function of the azimuthal angle, φ. The baseline sample S1 (one-step growth with instant reflectance oscillations) exhibited very anisotropic FWHMs for the on-axis (11$\underline{2}$2) XRCs, similar to previous reports.

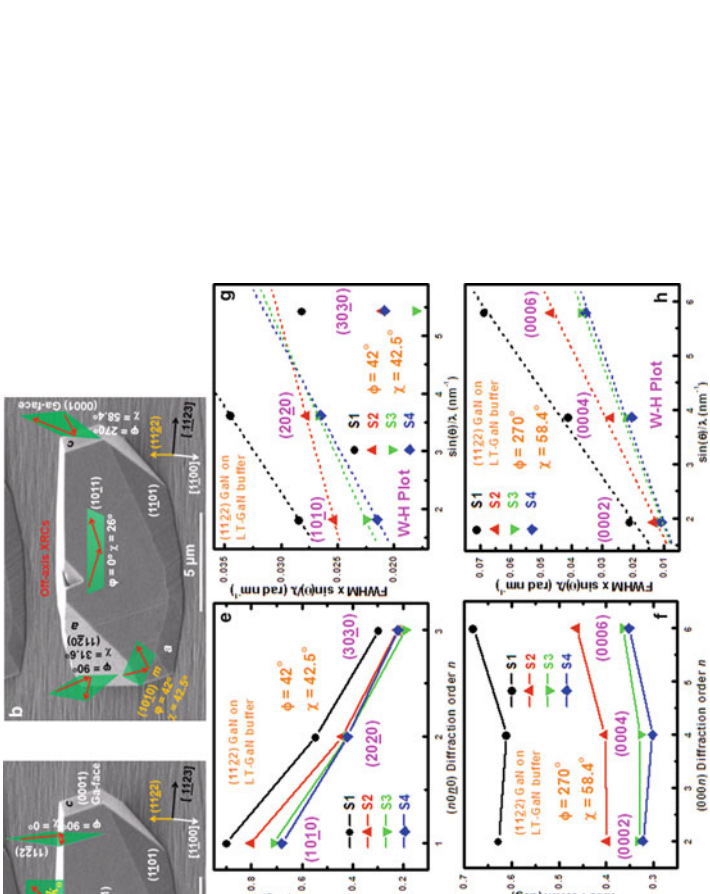

Fig. 1.14 SEM perspective side-view of a semipolar (11$\bar{2}$2) GaN SAG mesa labeled with orientations for the illustration of (**a**) on-axis and (**b**) off-axis XRC configurations. For $\varphi = 0$ and 90°, the X-ray rocking direction is parallel to [$\bar{1}$123] and the in-plane *m*-axis [1$\bar{1}$00], respectively. The incident and diffracted X-ray beams (*red arrows*) rock within a plane (shaded in *green*) for each diffraction plane with its index and orientation labeled in the vicinity. The (**a**) on-axis (11$\bar{2}$2) ($\chi = 0°$) and (**b**) off-axis planes ($\chi \neq 0°$), such as (10$\bar{1}$1), (10$\bar{1}$0), (11$\bar{2}$0), and (0002), were measured in symmetric and skew symmetric geometries, respectively. The FWHM of the (**c**) on-axis and (**d**) off-axis XRCs of semipolar (11$\bar{2}$2) GaN as a function of the azimuthal angle, φ. (**e**) The FWHMs of *m*-plane (*n*0$\bar{n}$0) XRCs ($n = 1$, 2, and 3). (**f**) The FWHMs of *c*-plane (000*n*) XRCs ($n = 2$, 4, and 6). (**g**) The modified WH plots of the *m*-plane (*n*0$\bar{n}$0) XRCs. The straight lines in (**g**) are the linear fits to the (10$\bar{1}$0) and (20$\bar{2}$0) data points of each (11$\bar{2}$2) GaN sample. (**h**) The modified WH plots of the *c*-plane (000*n*) XRCs

However, with the introduction of a 3D growth stage, the FWHM of the on-axis $(11\underline{2}2)$ XRC at $\varphi = 90°$ decreases monotonically from sample S1 to S4 by ~52%, and the FWHM-φ plots become less steep, indicative of improved microstructural quality with a greatly reduced anisotropy. All the BSFs (I_1, I_2, and E) are not visible under $(11\underline{2}2)$ diffraction, but the PDs can contribute to the broadening of the on-axis $(11\underline{2}2)$ XRCs. In addition, the $(11\underline{2}2)$ XRCs at $\varphi = 90°$ can also detect PSFs with a displacement vector of $1/2 < 10\underline{1}1 >$, which may be the dominant broadening factor to the $(11\underline{2}2)$ XRCs at $\varphi = 90°$ of sample S1.

In order to evaluate the effect of the two-step growth procedure on the mosaic twist (in-plane misalignment) within the $(11\underline{2}2)$ GaN films, we measured XRCs in a *skew* symmetric geometry for *off-axis* planes having an inclination angle χ with respect to the on-axis $(11\underline{2}2)$ at various azimuths (Fig. 1.14b). Figure 1.14d shows that from sample S1 to S4, the $(10\underline{1}1)$ and $(10\underline{1}0)$ XRCs were narrowed down by ~24%, and the $(11\underline{2}0)$ and (0002) XRCs by ~50%, which evidenced that the two-step growth technique could significantly improve the microstructural quality. It is noted that for all the samples, the XRC FWHMs of $(10\underline{1}0)$ and (0002) XRCs were much larger than that of $(11\underline{2}0)$ due to their different broadening factors [56]. It is known that $(11\underline{2}0)$ diffraction is not sensitive to the presence of BSFs, in contrast to $(10\underline{1}0)$ [41, 42].

As shown in Fig. 1.14e, as the diffraction order n increased from 1 to 3, the $(n0\underline{n}0)$ XRC FWHM decreased by ~67% for all the samples. The $(10\underline{1}0)$ XRCs were greatly broadened by BSFs [41, 42, 53, 57], although the X-ray rocking direction was not exactly along but at an angle to the c-axis. But the FWHMs ($0.2 \sim 0.3°$) of the $(30\underline{3}0)$ XRCs (insensitive to the presence of BSFs according to the visibility criteria [41, 42, 53, 57]) were fairly close to the dynamic range of the other off-axis XRCs linewidths (Fig. 1.14d). In contrast, as the diffraction order n increased, the c-plane $(000n)$ XRC FWHMs remained similar (Fig. 1.14f), which was because neither BSFs nor PSFs are visible under the $(000n)$ diffraction ($n = 2, 4$, and 6). Therefore, the c-plane XRCs were mainly broadened by PDs and/or perfect dislocations with Burgers vectors having a c-axis component. In the WH plots, the three data points of the $(000n)$ diffraction could be linearly fit by a straight line (Fig. 1.14h), but the $(30\underline{3}0)$ data points significantly deviated from the linear fits of the corresponding $(10\underline{1}0)$ and $(20\underline{2}0)$ data points (Fig. 1.14g) [41, 42, 53], which supported our assignment of the broadening mechanisms for the c- and m-plane XRCs.

From samples S1 to S4, the monotonic reduction of the m- and c-plane XRC FWHMs (Fig. 1.14c–f) indicated that a significant decrease in BSF and dislocation densities, respectively. It is believed that during the first-step 3D island growth, some dislocations bent at the inclined growth fronts [42, 58] and annihilated via their interaction with each other. And the reduction of BSF density in the semipolar $(11\underline{2}2)$ GaN films also comes from the blocking of BSFs by the lateral growth of tall mesas over small islands. The significant improvement of $(11\underline{2}2)$ GaN microstructural quality has led to bright photoluminescence (PL) of blue, green, green-yellow, and yellow $(11\underline{2}2)$ InGaN/GaN MQWs grown on GaN template (sample S4), as shown in Fig. 1.15. It should be mentioned that InGaN MQWs

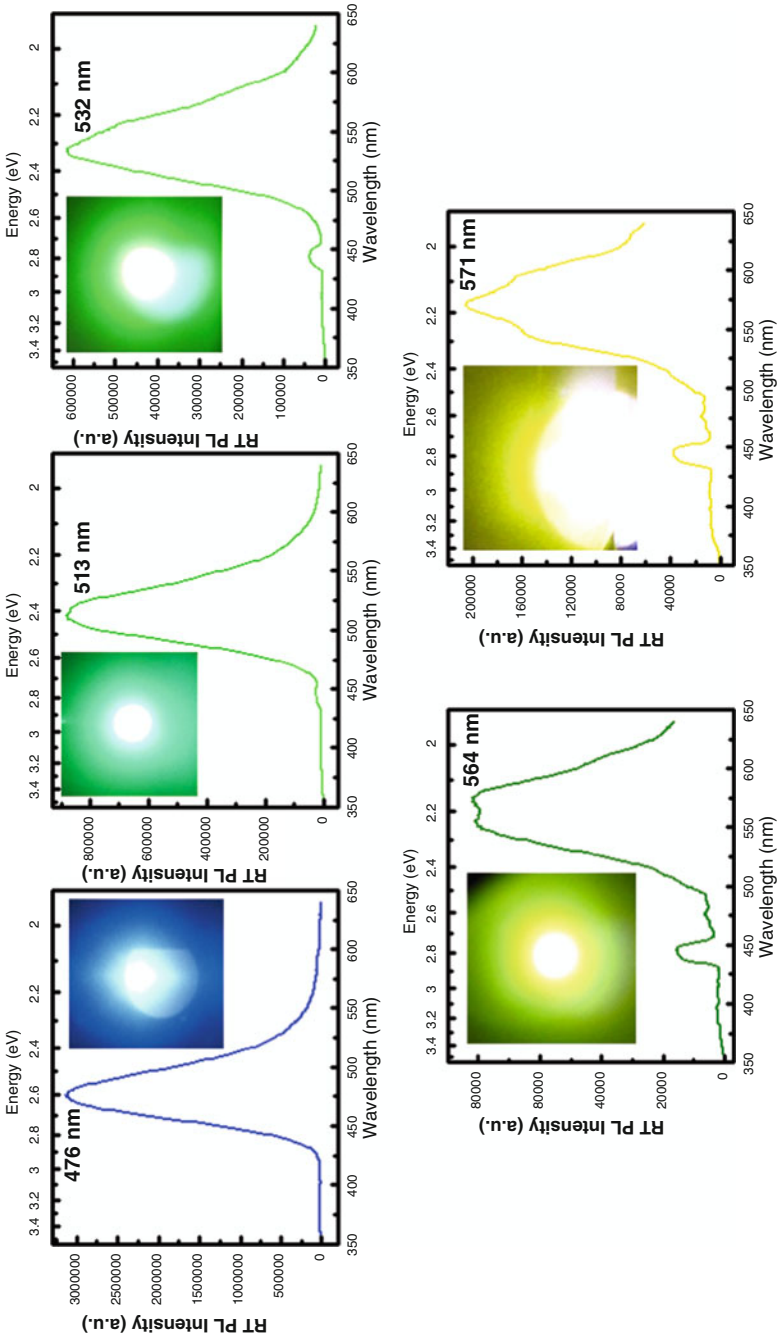

Fig. 1.15 Room temperature (RT) PL spectra of *blue*, *green*, *green–yellow*, and *yellow* semipolar (11$\bar{2}$2) InGaN/GaN MQWs, and their photos in the corresponding inset. The small peak near 445 nm was from the nonlasing line of the He-Cd laser

deposited on one-step grown (11$\underline{2}$2) GaN template (sample S1) did not give any emission because of the very high density of defects.

1.5 OCE of Semipolar GaN on Nonplanar Substrates

Due to the high density of extended defects (BSFs and PDs), semipolar (11$\underline{2}$2) InGaN/GaN MQWs and LEDs are still much dimmer than Ga-polar *c*-plane structures [3,59,60]. There have been various reports using ELOG to filter out part of the extended defects from the underlying GaN template, although the improvement of material quality is limited to only the Ga-face ELOG wings. It should be pointed out that, however, the defects in the template still penetrate into the mask opening regions, and moreover new BSFs and PDs are often generated in the N-face ELOG wings due to the interaction of the dielectric mask with the N-face growth front [47–49]. Thus, the ELOG GaN films have very limited useable area for device growth and fabrication.

A practical way of obtaining large-area SF-free nonpolar and semipolar GaN film is through OCE (Fig. 1.6d). The key innovation here is to decouple the nucleation orientation and the final coalesced surface orientation. To achieve this, sapphire substrate patterning, which so far has been mainly utilized to enhance light extraction, is required to expose certain facets (often *c*-plane) of sapphire for the nucleation of *c*-plane GaN with a good selectivity. Then the GaN stripes grown on the sapphire sidewall facets coalesce (often takes a long growth) into a continuous film with a nonpolar or semipolar surface orientation, depending on the geometric configuration between sapphire substrate and GaN film [61–65]. Patterned *r*-plane sapphire is an excellent platform for semipolar (11$\underline{2}$2) GaN, because the angle ($\sim$ 58°) between (0001) and (10$\underline{1}$2) of sapphire coincides with the angle (58.4°) between (0001) and (11$\underline{2}$2) of GaN (Fig. 1.6d) [64,65]. The OCE idea has also been successfully implemented to obtain nonpolar and semipolar GaN on patterned Si substrates [66–71].

The as-patterned *r*-sapphire (with no mask on the mesa) was thermally cleaned in H_2 at 1,100°C, followed by a deposition of a LT-AlN buffer at 500°C. The LT-AlN buffer was annealed during the temperature ramping up. The GaN growth was designed with three stages (1) to achieve selective nucleation of *c*-GaN on the sapphire sidewall facets (Fig. 1.16a), (2) to control the cross-section shape evolution of the GaN stripes to reach an ideal geometric configuration for coalescence (Fig. 1.16b), and (3) to have a rapid coalescence of the GaN stripes into a flat film (Fig. 1.16c). The *v*-plots of GaN (Fig. 1.4) again provided a very useful guidance in adjusting the growth conditions for the shaping and the coalescence of the stripes. A high reactor pressure and a low V/III ratio were used to promote the growth along the *c*-axis [0001] to block the BSFs and PDs in the N-face region of the neighboring stripes (Fig. 1.16b). A low reactor pressure and a relatively high V/III ratio were utilized to facilitate the stripe coalescence. The as-grown semipolar (11$\underline{2}$2) GaN film shows very narrow XRCs (not shown here) for all the on- and off-axis diffractions,

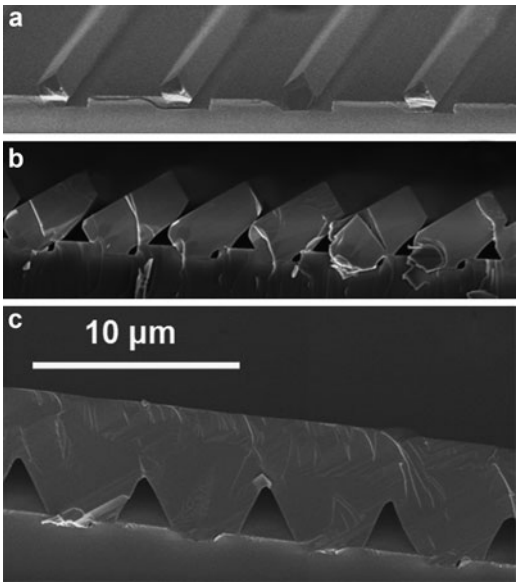

Fig. 1.16 OCE growth evolution of semipolar (11$\underline{2}$2) GaN on patterned *r*-plane sapphire. (**a**) selective nucleation of GaN on the sapphire *c*-plane sidewalls. (**b**) GaN stripes shaping for effective blocking of the BSFs and PDs in the neighboring stripes. (**c**) full coalescence of GaN stripes into a flat semipolar (11$\underline{2}$2) GaN film

with a linewidth ranging from 0.078 to 0.15°. The linewidths are about two- to fivefold narrower than those of the semipolar (11$\underline{2}$2) GaN grown on planar *m*-plane sapphire (Fig. 1.14), indicating a remarkable reduction in defect density, which is confirmed by TEM. In fact, the nearly BSF-free semipolar (11$\underline{2}$2) GaN film obtained on patterned *r*-plane sapphire has a crystalline quality comparable to that of *c*-plane GaN on *c*-plane sapphire. High brightness blue LEDs have been achieved on the semipolar (11$\underline{2}$2) GaN grown via OCE with a great spectral purity. The details of the semipolar (11$\underline{2}$2) GaN OCE growth and LED performance will be reported elsewhere.

1.6 Summary and Outlook

In this chapter, we highlighted the major challenges in the heteroepitaxy of nonpolar and semipolar GaN, poor surface morphology and microstructural defects, including BSFs and their associated PDs. Kinetic Wulff plots (*v*-plots) have been proven as a powerful tool in understanding and controlling GaN heteroepitaxy along various orientations. Based on the *v*-plots, a two-step growth scheme has been designed and implemented to improve the surface morphology and reduce the defect density through dislocation bending and BSF blocking for both nonpolar *a*-GaN and semipolar (11$\underline{2}$2) GaN. OCE as an emerging growth technology is producing device-quality heteroepitaxial semipolar GaN film, with a dislocation density comparable to that of *c*-GaN. Besides the approaches discussed earlier, SiN_x and ScN interlayers [30, 72] have also been reported as an effective method in filtering the BSFs and

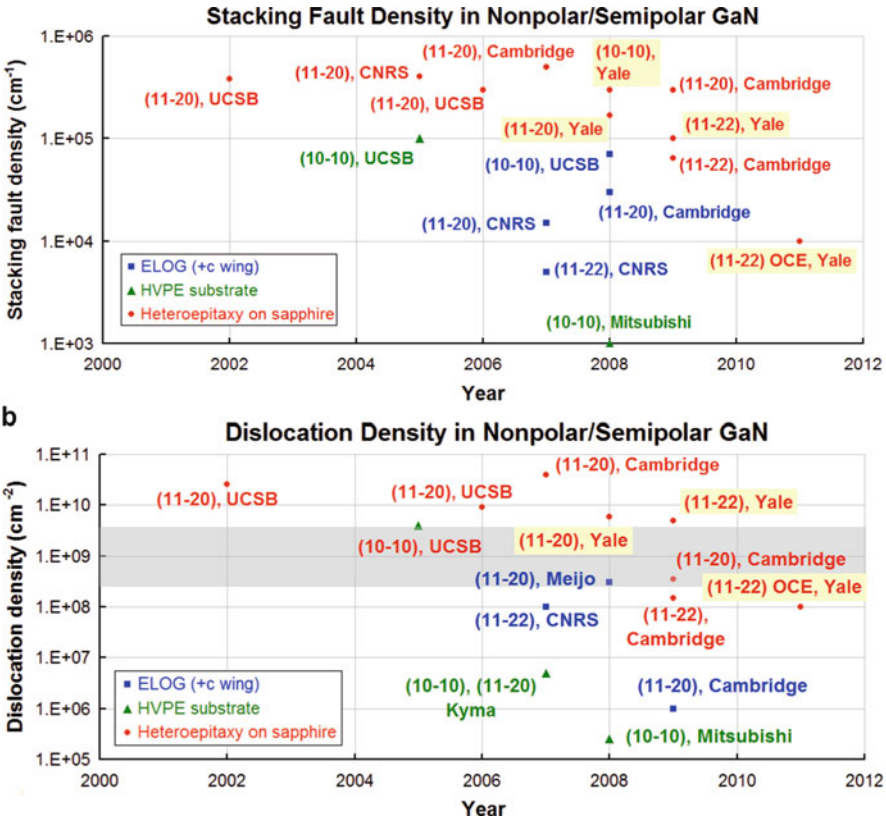

Fig. 1.17 Summary of the research timeline of nonpolar and semipolar GaN material quality: the density of BSFs (**a**) and dislocations (**b**). The *gray bar* in (**b**) indicates the typical range of threading dislocation density in heteroepitaxial *c*-plane GaN film [3]

PDs in nonpolar and semipolar GaN. The research timeline of nonpolar/semipolar GaN material quality by various groups is shown in Fig. 1.17. A combination of OCE and interlayers may be one of the ultimate solutions to further accelerate the research course of nonpolar and semipolar GaN (Fig. 1.1).

The performance gap between homoepitaxial and heteroepitaxial nonpolar/semipolar devices results from mainly the dramatic difference in defect density. The PDs bounding the BSFs are nonradiative recombination centers in nonpolar/semipolar GaN [73]. Therefore, most of the reported heteroepitaxial semipolar InGaN/GaN MQW LEDs were much dimmer than the Ga-polar *c*-plane LED grown under the same condition [3, 60]. The I–V characteristic of heteroepitaxial semipolar LED often exhibited a strong leakage behavior [3], which is probably related to the presence of the structural defects. In the long wavelength nonpolar/semipolar InGaN/GaN MQWs, the high strain can trigger the formation of new BSFs and PDs for both homoepitaxial and heteroepitaxial GaN substrates

[50, 51]. Moreover, in the semipolar (Al,In)GaN heterostructures, the (0001) slip plane is inclined with respect to the surface normal, and hence there is a component of shear stress on the slip plane which can cause misfit dislocation formation at the heterointerfaces [74–76]. The misfit dislocations together with the BSFs and PDs can further compromise the semipolar LED performance. Heteroepitaxial semipolar green LED wafer surface often appeared darkish when the growth temperature of *p*-GaN was high, indicating that the semipolar InGaN/GaN MQWs were not as robust as the *c*-plane MQWs against baking probably also due to the high density of extended defects. In addition, excess flow of Cp_2Mg is needed to achieve *p*-type $(11\underline{2}2)$ GaN because of the lower incorporation efficiency of Mg [77].

Acknowledgements This work was supported by the US DOE under Contract DE-FC26-07NT43227 and the US DOE office of Basic Energy Sciences under Contract DE-SC0001134. Christopher D. Yerino helped compiling the *v*-plots of GaN through consecutive SAG experiments under various growth conditions. Benjamin Leung carried out the OCE experiments for the growth of semipolar $(11\underline{2}2)$ GaN on patterned *r*-plane sapphire. The authors are thankful to Prof. Hyung Koun Cho and Mr. Bo Hyun Kong at Sungkyunkwan University (Korea) for their great help with the TEM measurements, and Dr. T.-S. Ko at National Chiao Tung University (Taiwan) for his help with the CL measurement.

References

1. H. Amano, N. Sawaki, I. Akasaki, Y. Toyoda, Appl. Phys. Lett. **48**, 353 (1986)
2. S. Nakamura, Jpn. J. Appl. Phys. Part 2 – Lett. **30**, L1705 (1991)
3. Q. Sun, J. Han, Proc. SPIE **7617**, 761717 (2010)
4. M.R. Krames, O.B. Shchekin, R. Mueller-Mach, G.O. Mueller, L. Zhou, G. Harbers, M.G. Craford, J. Disp. Technol. **3**, 160 (2007)
5. Y.C. Shen, G.O. Mueller, S. Watanabe, N.F. Gardner, A. Munkholm, M.R. Krames, Appl. Phys. Lett. **91**, 141101 (2007)
6. M.H. Kim, M.F. Schubert, Q. Dai, J.K. Kim, E.F. Schubert, J. Piprek, Y. Park, Appl. Phys. Lett. **91**, 183507 (2007)
7. P. Waltereit, O. Brandt, A. Trampert, H.T. Grahn, J. Menniger, M. Ramsteiner, M. Reiche, K.H. Ploog, Nature **406**, 865 (2000)
8. T. Takeuchi, H. Amano, I. Akasaki, Jpn. J. Appl. Phys. Part 1 – Regul. Pap. Short Notes Rev. Pap. **39**, 413 (2000)
9. S.-H. Park, J. Appl. Phys. **91**, 9904 (2002)
10. A.E. Romanov, T.J. Baker, S. Nakamura, J.S. Speck, J. Appl. Phys. **100**, 023522 (2006)
11. S.-H. Park, D. Ahn, Appl. Phys. Lett. **90**, 013505 (2007)
12. H. Shen, M. Wraback, H. Zhong, A. Tyagi, S.P. DenBaars, S. Nakamura, J.S. Speck, Appl. Phys. Lett. **95**, 033503 (2009)
13. M.C. Schmidt, K.C. Kim, H. Sato, N. Fellows, H. Masui, S. Nakamura, S.P. DenBaars, J.S. Speck, Jpn. J. Appl. Phys. Part 2 – Lett. Express Lett. **46**, L126 (2007)
14. H. Sato, R.B. Chung, H. Hirasawa, N. Fellows, H. Masui, F. Wu, M. Saito, K. Fujito, J.S. Speck, S.P. DenBaars, S. Nakamura, Appl. Phys. Lett. **92**, 221110 (2008)
15. N. Fellows, H. Sato, H. Masui, S.P. DenBaars, S. Nakamura, Jap. J. Appl. Phys. **47**, 7854 (2008)
16. K. Okamoto, J. Kashiwagi, T. Tanaka, M. Kubota, Appl. Phys. Lett. **94**, 071105 (2009)

17. Y. Enya, Y. Yoshizumi, T. Kyono, K. Akita, M. Ueno, M. Adachi, T. Sumitomo, S. Tokuyama, T. Ikegami, K. Katayama, T. Nakamura, Appl. Phys. Express **2**, 082101 (2009)
18. Y. Yoshizumi, M. Adachi, Y. Enya, T. Kyono, S. Tokuyama, T. Sumitomo, K. Akita, T. Ikegami, M. Ueno, K. Katayama, T. Nakamura, Appl. Phys. Express **2**, 092101 (2009)
19. J.S. Speck, S.F. Chichibu, MRS Bull. **34**, 304 (2009)
20. X. Li, X. Ni, J. Lee, M. Wu, U. Ozgur, H. Morkoc, T. Paskova, G. Mulholland, K.R. Evans, Appl. Phys. Lett. **95**, 121107 (2009)
21. J. Lee, X. Li, X. Ni, U. Ozgur, H. Morkoc, T. Paskova, G. Mulholland, K.R. Evans, Appl. Phys. Lett. **95**, 201113 (2009)
22. S.-P. Chang, T.-C. Lu, L.-F. Zhuo, C.-Y. Jang, D.-W. Lin, H.-C. Yang, H.-C. Kuo, S.-C. Wang, J. Electrochem. Soc. **157**, H501–H503 (2010)
23. S.-C. Ling, T.-C. Lu, S.-P. Chang, J.-R. Chen, H.-C. Kuo, S.-C. Wang, Appl. Phys. Lett. **96**, 231101 (2010)
24. K. Fujito, S. Kubo, I. Fujimura, MRS Bull. **34**, 313 (2009)
25. M.D. Craven, F. Wu, A. Chakraborty, B. Imer, U.K. Mishra, S.P. DenBaars, J.S. Speck, Appl. Phys. Lett. **84**, 1281 (2004)
26. M.D. Craven, S.H. Lim, F. Wu, J.S. Speck, S.P. DenBaars, Appl. Phys. Lett. **81**, 469 (2002)
27. X. Ni, Y. Fu, Y.T. Moon, N. Biyikli, H. Morko, J. Cryst. Growth **290**, 166 (2006)
28. Q. Sun, S.Y. Kwon, Z.Y. Ren, J. Han, T. Onuma, S.F. Chichibu, S. Wang, Appl. Phys. Lett. **92**, 051112 (2008)
29. Q. Sun, C.D. Yerino, Y. Zhang, Y.S. Cho, S.-Y. Kwon, B.H. Kong, H.K. Cho, I.-H. Lee, J. Han, J. Cryst. Growth **311**, 3824 (2009)
30. C.F. Johnston, M.A. Moram, M.J. Kappers, C.J. Humphreys, Appl. Phys. Lett. **94**, 161109 (2009)
31. T.J. Baker, B.A. Haskell, F. Wu, P.T. Fini, J.S. Speck, S. Nakamura, Jpn. J. Appl. Phys. Part 2 – Lett. Express Lett. **44**, L920 (2005)
32. T.J. Baker, B.A. Haskell, F. Wu, J.S. Speck, S. Nakamura, Jpn. J. Appl. Phys. Part 2 – Lett. Express Lett. **45**, L154 (2006)
33. P. Vennegues, Z. Bougrioua, T. Guehne, Jpn. J. Appl. Phys. Part 1 – Regul. Pap. Brief Commun. Rev. Pap. **46**, 4089 (2007)
34. K. Hiramatsu, K. Nishiyama, A. Motogaito, H. Miyake, Y. Iyechika, T. Maeda, Phys. Stat. Sol. A **176**, 535 (1999)
35. D.X. Du, D.J. Srolovitz, M.E. Coltrin, C.C. Mitchell, Phys. Rev. Lett. **95**, 155503 (2005)
36. Q. Sun, C.D. Yerino, T.S. Ko, Y.S. Cho, I.H. Lee, J. Han, M.E. Coltrin, J. Appl. Phys. **104**, 093523 (2008)
37. Y.S. Cho, Q. Sun, I.H. Lee, T.S. Ko, C.D. Yerino, J. Han, B.H. Kong, H.K. Cho, S. Wang, Appl. Phys. Lett. **93**, 111904 (2008)
38. Y.J. Sun, O. Brandt, U. Jahn, T.Y. Liu, A. Trampert, S. Cronenberg, S. Dhar, K.H. Ploog, J. Appl. Phys. **92**, 5714 (2002)
39. T.Y. Liu, A. Trampert, Y.J. Sun, O. Brandt, K.H. Ploog, Philos. Mag. Lett. **84**, 435 (2004)
40. A. Trampert, T.Y. Liu, O. Brandt, K.H. Ploog, J. Phys. IV, **132**, 221 (2006)
41. Q. Sun, T.S. Ko, C.D. Yerino, Y. Zhang, I.H. Lee, J. Han, T.-C. Lu, H.-C. Kuo, S.-C. Wang, Jap. J. Appl. Phys. **48**, 071002 (2009)
42. Q. Sun, B.H. Kong, C.D. Yerino, T.-S. Ko, B. Leung, H.K. Cho, J. Han, J. Appl. Phys. **106**, 123519 (2009)
43. J.L. Hollander, M.J. Kappers, C. McAleese, C.J. Humphreys, Appl. Phys. Lett. **92**, 101104 (2008)
44. T.S. Ko, T.C. Wang, R.C. Gao, H.G. Chen, G.S. Huang, T.C. Lu, H.C. Kuo, S.C. Wang, J. Cryst. Growth **300**, 308 (2007)
45. Y. Dikme, P.V. Gemmern, B. Chai, D. Hill, A. Szymakowski, H. Kalisch, M. Heuken, R.H. Jansen, Phys. Stat. Sol. (c) **2**, 2161 (2005)
46. D.N. Zakharov, Z. Liliental-Weber, B. Wagner, Z.J. Reitmeier, E.A. Preble, R.F. Davis, Phys. Rev. B **71**, 235334 (2005)

47. B.A. Haskell, F. Wu, M.D. Craven, S. Matsuda, P.T. Fini, T. Fujii, K. Fujito, S.P. DenBaars, J.S. Speck, S. Nakamura, Appl. Phys. Lett. **83**, 644 (2003)
48. B.A. Haskell, T.J. Baker, M.B. McLaurin, F. Wu, P.T. Fini, S.P. DenBaars, J.S. Speck, S. Nakamura, Appl. Phys. Lett. **86**, 111917 (2005)
49. T. Guhne, Z. Bougrioua, P. Vennegues, M. Leroux, M. Albrecht, J. Appl. Phys. **101**, 113101 (2007)
50. Z.H. Wu, T. Tanikawa, T. Murase, Y.Y. Fang, C.Q. Chen, Y. Honda, M. Yamaguchi, H. Amano, N. Sawaki, Appl. Phys. Lett. **98**, 051902 (2011)
51. F. Wu, Y.-D. Lin, A. Chakraborty, H. Ohta, S.P. DenBaars, S. Nakamura, J.S. Speck, Appl. Phys. Lett. **96**, 231912 (2010)
52. Q. Sun, Y.S. Cho, I.H. Lee, J. Han, B.H. Kong, H.K. Cho, Appl. Phys. Lett. **93**, 131912 (2008)
53. M.B. McLaurin, A. Hirai, E. Young, F. Wu, J.S. Speck, Jpn. J. Appl. Phys. **47**, 5429 (2008)
54. T. Wernicke, C. Netzel, M. Weyers, M. Kneissl, Phys. Stat. Sol. (c) **5**, 1815 (2008)
55. P. Vennegues, T. Zhu, D. Martin, N. Grandjean, J. Appl. Phys. **108**, 113521 (2010)
56. Q. Sun, B. Leung, C.D. Yerino, Y. Zhang, J. Han, Appl. Phys. Lett. **95**, 231904 (2009)
57. M.A. Moram, C.F. Johnston, J.L. Hollander, M.J. Kappers, C.J. Humphreys, J. Appl. Phys. **105**, 113501 (2009)
58. X. Ni, U. Ozgur, A.A. Baski, H. Morkoc, L. Zhou, D.J. Smith, C.A. Tran, Appl. Phys. Lett. **90**, 182109 (2007)
59. M.J. Kappers, J.L. Hollander, C. McAleese, C.F. Johnston, R.F. Broom, J.S. Barnard, M.E. Vickers, C.J. Humphreys, J. Cryst. Growth **300**, 155 (2007)
60. P.D. Mierry, T. Guehne, M. Nemoz, S. Chenot, E. Beraudo, G. nataf, Jpn. J. Appl. Phys. **48**, 031002 (2009)
61. N. Okada, Y. Kawashima, K. Tadatomo, Appl. Phys. Express **1**, 111101 (2008)
62. K. Okuno, Y. Saito, S. Boyama, N. Nakada, S. Nitta, R.G. Tohmon, Y. Ushida, N. Shibata, Appl. Phys. Express **2**, 031002 (2009)
63. Y. Saito, K. Okuno, S. Boyama, N. Nakada, S. Nitta, Y. Ushida, N. Shibata, Appl. Phys. Express **2**, 041001 (2009)
64. N. Okada, A. Kurisu, K. Murakami, K. Tadatomo, Appl. Phys. Express **2**, 091001 (2009)
65. P. de Mierry, N. Kriouche, M. Nemoz, S. Chenot, G. Nataf, Appl. Phys. Lett. **96**, 231918 (2010)
66. Y. Honda, N. Kameshiro, M. Yamaguchi, N. Sawaki, J. Cryst. Growth **242**, 82 (2002)
67. T. Hikosaka, T. Tanikawa, Y. Honda, M. Yamaguchi, N. Sawaki, Phys. Stat. Sol. (c) **5**, 2234 (2008)
68. N. Sawaki, T. Hikosaka, N. Koide, S. Tanaka, Y. Honda, M. Yamaguchi, J. Cryst. Growth **311**, 2867 (2009)
69. M. Yang, H.S. Ahn, T. Tanikawa, Y. Honda, M. Yamaguchi, N. Sawaki, J. Cryst. Growth **311**, 2914 (2009)
70. T. Tanikawa, D. Rudolph, T. Hikosaka, Y. Honda, M. Yamaguchi, N. Sawaki, J. Cryst. Growth **310**, 4999 (2008)
71. N. Sawaki, Proc. SPIE **7279**, 727902 (2009)
72. C.F. Johnston, M.J. Kappers, M.A. Moram, J.L. Hollander, C.J. Humphreys, J. Cryst. Growth **311**, 3295 (2009)
73. A.Y. Polyakov, N.B. Smirnov, A.V. Govorkov, H. Amano, S.J. Pearton, I.H. Lee, Q. Sun, J. Han, S.Y. Karpov, Appl. Phys. Lett. **98**, 072104 (2011)
74. A. Tyagi, F. Wu, E.C. Young, A. Chakraborty, H. Ohta, R. Bhat, K. Fujito, S.P. DenBaars, S. Nakamura, J.S. Speck, Appl. Phys. Lett. **95**, 251905 (2009)
75. F. Wu, A. Tyagi, E.C. Young, A.E. Romanov, K. Fujito, S.P. DenBaars, S. Nakamura, J.S. Speck, J. Appl. Phys. **109**, 033505 (2011)
76. E.C. Young, F. Wu, A.E. Romanov, A. Tyagi, C.S. Gallinat, S.P. DenBaars, S. Nakamura, J.S. Speck, Appl. Phys. Express **3**, 011004 (2010)
77. S.C. Cruz, S. Keller, T.E. Mates, U.K. Mishra, S.P. DenBaars, J. Cryst. Growth **311**, 3817 (2009)

Chapter 2
High-Quality Al-Rich AlGaN Alloys

B.N. Pantha, J.Y. Lin, and H.X. Jiang

Abstract A review is given of the synthesis and characterization of high Al-content AlGaN thin films, including optical properties, bandgap bowing, exciton localization, and n- and p-type doping. A summary of energy levels for various acceptors in AlN is also given.

2.1 Introduction

AlGaN alloys have the capability of tuning the direct bandgap over a large energy range, from around 3.4–6.1 eV, making them very useful for ultraviolet (UV) and deep ultraviolet (DUV) optoelectronic device applications with operating wavelength down to 200 nm [1–7]. The bandgap of AlGaN alloys can be adjusted by varying Al content so the visible/solar-blind UV detectors with variable cutoff wavelengths can be fabricated without the use of extra filters. Other potential applications of Al-rich AlGaN-based devices include high-density optical data storage, fluorescence detection of chemical and biological agents, water and air purification, medical research, and healthcare. GaN-based devices have already been commercialized and are important materials in the fields of compound semiconductors and optoelectronic devices. However, many fundamental properties of Al-rich AlGaN alloys are still not fully understood.

The growth of Al-rich AlGaN alloys is challenging due to the large bond strength between the Al and N atoms compared to that between the Ga and N atoms. This strong bonding results in reduced surface mobility of the Al species, making it challenging to achieve step flow growth [8, 9]. Because of this, AlN- and Al-rich AlGaN alloys are generally synthesized at higher growth temperatures than GaN

B.N. Pantha · J.Y. Lin (✉) · H.X. Jiang (✉)
Department of Electrical and Computer Engineering, Texas Tech University, Lubbock, TX 79409, USA
e-mail: hx.jiang@ttu.edu; jingyu.lin@ttu.edu

S. Pearton (ed.), *GaN and ZnO-based Materials and Devices*,
Springer Series in Materials Science 156, DOI 10.1007/978-3-642-23521-4_2,

using metal organic chemical vapor deposition (MOCVD). Low growth pressure and V/III ratio are normally chosen to avoid undesired parasitic reactions at high temperatures. Indium as a surfactant has also been investigated to increase the surface mobility of Al atoms, reduce dislocation density, and enhance the n-type conductivity in Al-rich AlGaN alloys [10–15].

III-nitride materials and devices are usually grown on *c*-plane sapphire and SiC substrates. Due to the large piezoelectric field, quantum well (QW) structures grown on *c*-plane sapphire or SiC substrates with certain well thickness may suffer from the quantum confined stark effect (QCSE) [16–21]. This in turn causes spatial separation of electron and hole wave functions in QWs and reduces radiative recombination efficiency. Furthermore, devices consisting of Al-rich AlGaN and grown on polar substrates significantly reduce the surface emission intensity as Al content increases since the dominant emission in Al-rich AlGaN has a polarization of $\mathbf{E}\|\mathbf{c}$[22, 23]. This difference in band structures between GaN and AlN causes the polarization dependence emission in AlGaN alloys. Therefore, growth of DUV devices on nonpolar AlN templates such as *a*-plane AlN/*r*-plane sapphire, *m*-plane AlN/*m*-plane SiC, and *m*-plane AlN/*m*-plane AlN substrates have attracted large attention because of the absence of polarization fields and enhanced surface emission [16, 24–37].

AlN and GaN are completely miscible. Thus, AlGaN alloys in the entire compositional range have been successfully synthesized and investigated [38–43]. Compositional and temperature dependences of the energy bandgap bowing parameter and optical transitions have been extensively studied [44–49]. Due to the advances in growth and characterization methods, these parameters are now known more accurately. For example, recent studies have found the value of the bandgap bowing parameter was in a narrower variation range compared to those from previous reports ($b \sim$ 0.6–1.3 eV vs. –0.8 to 2.6 eV) [41, 50]. This accuracy is attributed to the availability of wide compositional range AlGaN alloys with high-quality epitaxial layers. The knowledge of compositional dependence of AlGaN alloys is essential to the design of AlGaN/GaN QW devices.

Other important properties which affect the optical and electrical properties of AlGaN alloys are carrier and exciton localizations. Exciton localization energy and PL emission linewidth yield information about compositional and potential fluctuations occurring in semiconductor alloys. Fundamental optical properties such as optical transitions, carrier dynamic processes, and carrier–phonon interactions predominantly determine the device performance. Therefore, understanding fundamental optical properties is crucial for the development of suitable material qualities and device structures [22, 50–62].

Control of electrical conductivity in Al-rich $Al_xGa_{1-x}N$ alloys ($x > 0.7$) is still challenging. Silicon has been widely studied for n-type doping in Al-rich AlGaN alloys, which are intrinsically insulating. The deepening of Si donor levels is one of the main reasons for low electrical conductivity of high Al content AlGaN [63–69]. Another major difficulty in obtaining highly conductive n-type Al-rich AlGaN alloys is compensation of electrons by cation vacancies $(V_{III})^{3-}$ and their complexes. It has been recognized that suppressing these intrinsic defects could

significantly improve the conductivity and material quality of Al-rich AlGaN alloys [63–69]. Resistivity as low as 0.0075Ω cm has been obtained in $Al_{0.7}Ga_{0.3}N$: Si by suppressing these defects [65, 66].

Mg is the most widely investigated dopant for p-type doping in III-nitride semiconductors. However, the deep nature of Mg acceptors, (160 meV for GaN and 510–600 meV for AlN) especially in Al-rich AlGaN alloys, is the main reason of not achieving room temperature p-type conductivity [70–76, 78]. Searches for alternative doping elements such as Be, Zn, and C have also been attempted with limited success [62, 63]. In this chapter, we cover the recent progresses in growth, optical and electrical properties of high-quality Al-rich AlGaN alloys.

2.2 Growth of AlGaN

2.2.1 Typical Growth Condition of AlGaN

High-quality AlGaN alloys with high Al contents are generally grown by MOCVD on *c*-plane sapphire (Al_2O_3) substrates. SiC, bulk AlN, and Si substrates have also attracted research interest in the recent years. Trimethyl aluminum (TMAl), trimethyl gallium (TMGa), and NH_3 are used as Al, Ga, and N sources, respectively. General MOCVD growth conditions for InN, GaN, and AlN are illustrated in Fig. 2.1. Compared to InN or GaN, AlN is grown at a higher growth temperature (∼1, 300 °C) due to short migration of Al species at low growth temperature [8]. Low growth pressure and V/III ratio are normally chosen to avoid unwanted parasitic reaction between metal organic precursors and NH_3, which is prominent at high temperatures.

Okada et al. [9] studied the thermodynamic aspects of growing high Al content AlGaN by MOCVD. They investigated the effect of V/III ratio and growth temperature on incorporation of Al content in AlGaN. The results of their investigation are shown in Fig. 2.2. Lines denote the calculation results while scattered points are

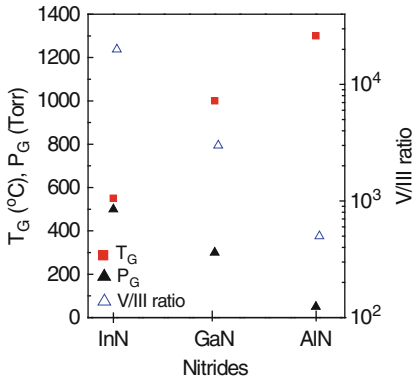

Fig. 2.1 Typical growth conditions for InN, GaN, and AlN. Growth conditions such as high growth temperature, low growth pressure, and low V/III ratio are the most conventionally used conditions to grow Al-rich AlGaN by MOCVD

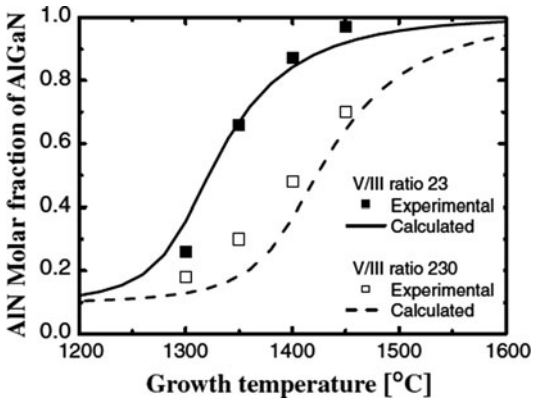

Fig. 2.2 Effect of V/III ratio on Al incorporation in GaN (after [9])

experimental data. They found that incorporation of Al content is strongly affected by V/III ratio. With fixed growth temperature, lower V/III ratio resulted AlGaN in higher Al content. In order to get similar Al content with higher V/III ratios, the growth temperature needs to be raised. The experimental results matched well with the calculated results. The reason for low incorporation efficiency of Al with higher V/III ratios is that the equilibrium partial pressure of Ga increases with an increase of V/III ratio compared to that of Al. On the other hand, equilibrium constants (see [9] for details) increase with an increase of growth temperature so that the partial pressure of Ga deceases. At high growth temperatures, the partial pressure of Ga is much lower than that of Al and hence, Al content increases with increasing of temperature. The AlGaN alloys grown at high temperatures were found to be of high quality.

2.2.2 Effect of In as Surfactant in Al-Rich AlGaN Alloys

2.2.2.1 Electrical Conductivity

Highly conductive n-type Al-rich AlGaN alloys are very difficult to achieve due to the higher activation energy of Si impurity (donor) and the generation of cation vacancy $(V_{III})^{3-}$ and cation vacancy complexes $(V_{III}\text{-complex})^{2-}$ during the growth [51, 59, 60, 64–68, 70–73, 79]. Dislocations may also introduce acceptor-like centers through dangling bonds along the dislocation line [80]. Indium–silicon codoping of Al-rich AlGaN layers at relatively low temperatures $\sim$ (920–950°C) have been reported to result in high electron concentrations and low resistivity [10, 12]. It is believed that indium incorporation can reduce threading dislocation (TD) density [13], resulting in suppression of dislocation-induced compensation sites and thus increase electrical conductivity. Indium may also counteract the incorporation of defects responsible for self-compensation in Al-rich AlGaN layers, such as DX centers, cation vacancies, and their complexes [14].